# WhirlWind

## Wind Energy Harvesting Wireless System for Sensing Angle of Attack and Wind Speed

**Suryansh Sharma**

Embedded and Networked Systems Group,
Faculty of Electronics Engineering, Mathematics and Computer Science,
Delft University of Technology, The Netherlands

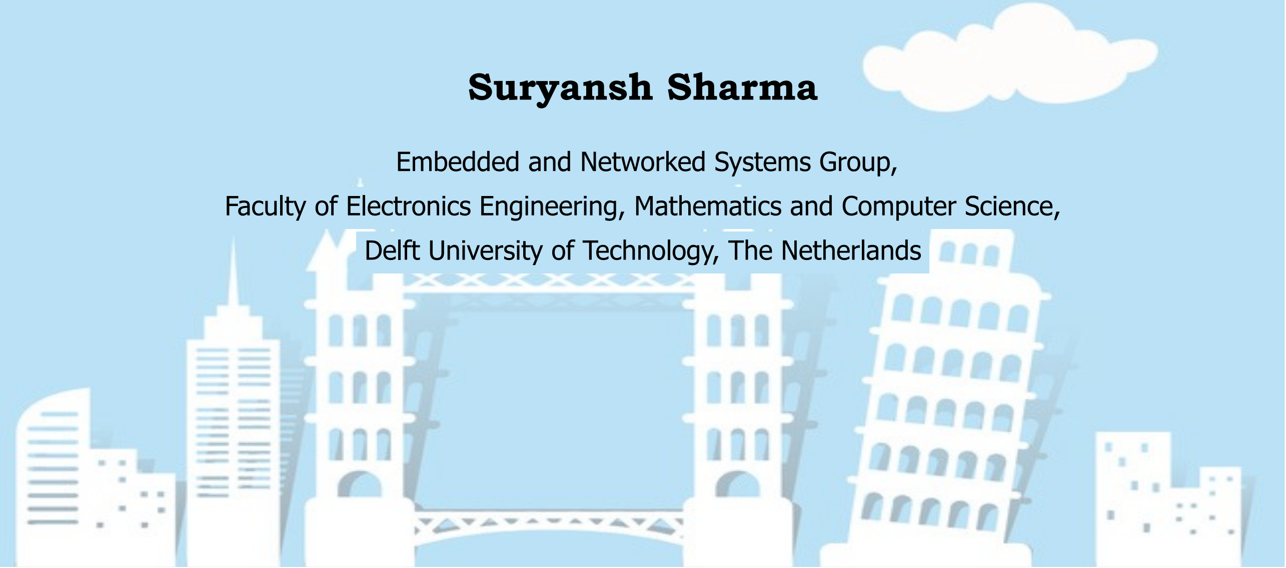

This thesis has been approved by

Supervisor: Dr. R.V. Prasad

Thesis Committee:

| | |
|---|---|
| Dr. ir. C.J.M Verhoeven, | Technische Universiteit Delft |
| Dr. ir. Arjan Van Genderen, | Technische Universiteit Delft |
| Dr. R.V. Prasad, | Technische Universiteit Delft |

This work was made possible through the 4TU data refinement grant administered by the 4TU coalition in The Netherlands.

*Keywords:* Wind energy harvesting, angle of attack sensor, wind speed sensor, piezoelectric, batteryless, aeroelastic flutter

*Whatever you want to do,*
*if you do it with all of your heart, it will happen.*

William Kamkwamba,
The Boy Who Harnessed The Wind

# Acknowledgements

*Don’t let the sun go down without saying thank you to someone, and without admitting to yourself that absolutely no one gets this far alone.*

Stephen King

I am indebted to many people whose belief, contributions and advice has led to the development of the work presented herein.

I would like to extend my heartfelt gratitude to Professor R.V. Prasad (VP) for this constant supervision and faith in this endeavour. I would also like to thank Ashutosh Simha, Vineet Gokhale and Sujay Narayana for their invaluable advice on and support for this work. I am also grateful to Professor Vos who brought our attention to such an interesting problem and was instrumental in getting access to the testing facilities. I am also thanful to Emiel from the Low Speed Wind Tunnel Laboratory and Dimple Aerospace, B.V. who guided me in my maiden experiments in the wind tunnel as well as the Delft Open Hardware community (Jose, Santosh, Jerry, Jannes and Andrea) whose enthusiasm and help cannot be left unmentioned.

I am deeply appreciative to my friends and peers who encouraged and pushed me even in these trying and uncertain times. Thank you, Turkuaz and Alois for making me feel like family. You both mean a lot to me. I want to thank Edward, Chiara, Roderick, Matthijs for all the wonderful moments throughout these past months. I also would like to thank Vladislava for being the beacon of hope and support in this journey. You helped me more than you can imagine.

I am forever indebted to my brother, Ayush Sharma, whose resolve and support has echoed throughout my life. Finally, and most importantly I would like to thank my mother, Sushama Sharma who instilled in me the maxim that people who do not stop trying, can never fail. Thank you everybody for the love, faith and support.

Suryansh Sharma
August 21, 2020

# Contents

# List of Figures

# List of Tables

# Abstract

Air travel has become considerably safe in the last decades, yet we see some fatal accidents. Some recent incidents reveal that there are issues in the measurement of wind speed and angle of attack (AoA). This paper presents a novel system for concurrently sensing the wind speed and AoA of an aircraft. We present the design of a wireless sensor, called *Hermes*, that simultaneously enables sensing as well as piezoelectric energy harvesting, making it self-powered and batteryless. Hermes comprises of a set of piezoelectric films which flutter due to incoming wind speed, and the characteristic of this aeroelastic flutter is utilized for determining the wind speed and AoA of the incoming airflow. The design of Hermes is such that sensing performance and energy harvesting capability are simultaneously maximized, without the need for trading off.

Hermes, a small form factor electronic module along with piezoelectric films and a 3D mount, is fabricated, tested in a wind tunnel, and in a real aircraft fuselage for its communication performance. Hermes harvests an average power of 440 $\mu$W power. Over a wide range of AoA of $-10^\circ$ to $30^\circ$, the estimation of the wind speed is within 0.2 m/s error with 90% probability and AoA error is within $1.2^\circ$ with $90\%$ probability. Hermes can be used in light aircraft and long endurance UAVs as is. It can also be used in several other applications, such as windmills. Hermes is expected to open up new avenues for interdisciplinary research for aerospace applications.

# 1

# Introduction

## 1.1. Motivation

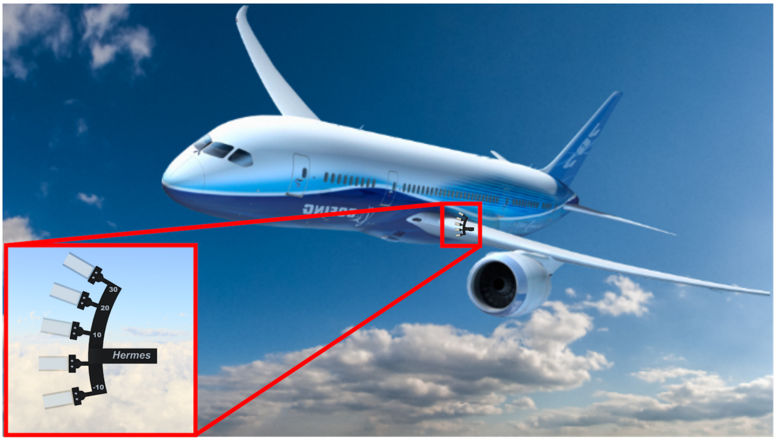

Figure 1.1: Conceptual view of the proposed wind energy harvesting, wireless sensing system for AoA and wind speed.

In this work, we present a novel, wind energy harvesting, piezoelectric based, batteryless and wireless sensor for reliable and simultaneous measurement of Angle of Attack (AoA) and wind speed for increased safety and redundancy in aircraft. Fig. 1.1 depicts a conceptual view of the proposed system.

The last decade has witnessed countless aerospace innovations involving sensors and systems, which indeed solved many challenges and overcame many obstacles [4, 5]. Yet, the airline industry has witnessed several dreadful accidents resulting in tremendous loss of lives [6]. Apart from pilot errors, many such accidents are attributed to sensor malfunctions, inaccuracies, and lack of redundancy (multiple sensors) in the system [7, 8]. This calls for innovation in sensor systems that can reduce fatalities even further from ≈13 in 1 M and 6.5 in 1 M flight departures in 2018 and 2019, respectively[9], and make flying the safest mode of transportation.

**What went wrong?** Air France flight Airbus A330 flying from Rio de Janeiro, Brazil, to Paris, France on 1 June 2009 stalled and failed to recover, and finally crashed into the Atlantic Ocean[10]. Lion Air flight 610 on October 29, 2018 and Ethiopian Airlines flight 302 on March 10, 2019, also encountered fatal crashes of the Boeing 737 Max 8. According to a preliminary report [11], one of the primary causes was autopilot failure which resulted from erroneous AoA measurements. Boeing has also reported this aspect and also highlights the risks associated with the current standard practice of estimating AoA in aircraft [12].

AoA is a fundamental aerodynamic parameter defined as the angle between the reference line of an airborne body (which is traditionally the chord line of an airfoil) and the relative wind velocity vector (see Fig. 1.2). Accurate measurement of AoA along with the wind speed is crucial for maintaining appropriate lift and preventing stall regimes during take-off, landing, and cruise [13]. The sensors for these have played instrumental roles in realizing the human desire to fly, starting from the advent of the first human aircraft in 1903 [14]. Although these sensors have been integral elements of aircraft and UAVs since a century, even today they are prone to inaccuracies and faulty measurements.

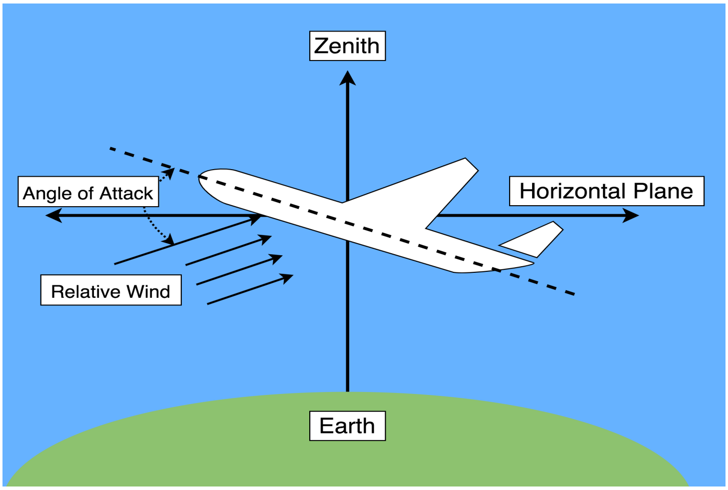

Figure 1.2: Angle of Attack made by an aircraft.

## 1.2. Design challenges

The problem of designing sensors for simultaneous and reliable measurement of AoA and wind speed is nontrivial. The design of the sensor should be general-purpose and possess the potential to be adapted widely. To this end, we list here the foremost challenges:

1. *Energy Harvesting*: Any new system developed for aircraft requires wiring to supply power from the main battery. Thus, self-powered design is crucial in increasing the reliability of the sensor even during a system malfunction or catastrophic failure in other systems of the aircraft.
2. *Range and accuracy*: AoA manifests a broad range of 40° and requires a high resolution of 1° [15]. Designing a sensor to sense over wide range with high accuracy is a challenge.
3. *Form factor*: The sensor should be of small form-factor, thus making it convenient and easy to mount on the airfoil of a carrier airplane or a fixed-wing/VTOL UAV with minimal overhead in terms of weight. Further, for broader applicability, the sensors should be capable of retrofitting.
4. *Reliability versus cost*:] Deploying redundant sensors would lead to better accuracy and reliability, however, these improvements inevitably increase the cost.
5. *Low-power radio communication*: To avoid inherent problems with wired communication, such as the requirement of cables and a power-source, communication with the sensors needs to be carried out via radio link that utilizes only the harvested energy.
6. *Robustness and computational simplicity*: AoA and wind speed fluctuate vigorously over a wide range, especially during take-off and landing. Therefore, the estimation algorithms should be robust to these variations and also computationally viable to be implemented on a low-power microcontroller.
7. *Simultaneous measurement*: Separate sensors for AoA and wind speed increase the bulk of measuring unit, whereas measuring one quantity and inferring the other leads to inaccuracies. Systems for simultaneously measuring the two quantities are required.

Literature provides a few works that have addressed some of the above challenges [16, 17]. However, they fall short of addressing one or some of the issues mentioned above. These severe limitations in the state of the art inspire us to come up with a novel sensor design. The question we address in this paper is: **Is there a simple, one-stop solution that addresses the challenges mentioned above?**

In this paper, we present *Hermes*[1] – a wind-powered, wireless sensor for reliable and robust measurement of AoA and wind speed. A first of its kind sensor, Hermes leverages as a source of energy the very physical phenomenon that it is designed to measure – the wind speed. Hermes employs piezoelectric films to utilize *flutter*, a destructive phenomenon[2] that is inevitably introduced by wind, to accurately sense AoA and wind speed as well as harvest energy completely avoiding the use of batteries. In addition to the above challenges, Hermes is amicable to retrofitting, thereby exhibiting compatibility without regard to the specifications of the aircraft/UAV and operational conditions.

## 1.3. Contributions

Our primary contributions in this paper are summarized here:

1. We present *Hermes*, which is a wind-powered, wireless, and cost-effective novel solution – a first of its kind – for robust and reliable measurement of AoA and wind speed. We provide details on the complete system and design principle along with its mechanical and electrical characterization.
2. We have built a 3D printed Hermes sensor unit with mounting, along with a low form factor electronics, for testing it extensively.
3. This work being interdisciplinary, we provide the necessary background on the working principle of the piezoelectric film flutter in a fluid environment that has not been attempted hitherto for sensing applications.
4. We develop an empirical model of AoA and wind speed sensing through flutter and piezoelectric voltage characterization.
5. We propose *Nonlinear Surface Regression* (NSR) – a computationally inexpensive, real-time algorithm for simultaneous and accurate estimation of AoA and wind speed using the same sensing mechanism.
6. We conduct an extensive performance evaluation of Hermes in a wind tunnel and also study its effectiveness in communicating its information in a real aircraft fuselage. In both settings, our findings reveal high accuracy.

## 1.4. Organization

The remainder of the paper is organized as follows. In Section 2, we brief the necessary background from fluid dynamics that are central to understanding the design and working of Hermes. In Section 3, we perform the methodology of characterization of the piezoelectric films used by Hermes, and in Section 4, we present our findings. In Section 5, we present details on the system design of Hermes as well as the sensing algorithms. In Section 6, we carry out extensive performance

---

[1] Named after the ancient Greek god of travelers.

[2] The term **WhirlWind** represents this aspect of our sensor design.

evaluation of Hermes, followed by discussions in Section 7. In Section 8, we discuss state of the art in AoA and wind speed sensing and state our conclusions in Section 9.

# 2

# Theoretical Foundation

In this section, we provide theoretical background that is necessary for understanding the design of Hermes.

## 2.1. Aeroelastic flutter: A destructive ally

Aeroelastic flutter is one of the many aeroelastic phenomena that occur in dynamic fluid-structure interactions. Flutter has traditionally been deemed as a *destructive* phenomenon in the domain of aeroelasticity and is considered as a highly nonlinear problem due to the large strains and geometric deformations that it causes as well as due to its transient behaviour [18]. Flutter originates from the aeroelastic instability of a compliant structure[1], for instance, a flexible sheet immersed in a flowing fluid. An elastic plate, when placed in an axial fluid flow begins to flutter above the critical velocity of the fluid, where the destabilizing forces overpower the stabilizing effect of the rigidity of the structure [19].

We can leverage this phenomenon to harvest energy from the flow field (wind in our case). The idea is to translate fluid kinetic energy using flutter into the strain energy of the structure. This strain energy can then be harvested into usable electrical energy via the piezoelectric effect of the film. Fig. 2.1 shows this energy harvesting strategy.

Different classifications of flutter types were made in [20, 21] which are based on the excitation and flutter sustenance mechanisms. The two types most relevant to wind energy harvesting are:

1. Extraneously-Induced Excitation (EIE)
2. Movement-Induced Excitation (MIE)

---

[1] We use this standard terminology from the aerospace domain, however, in this work, it refers to the piezoelectric film.

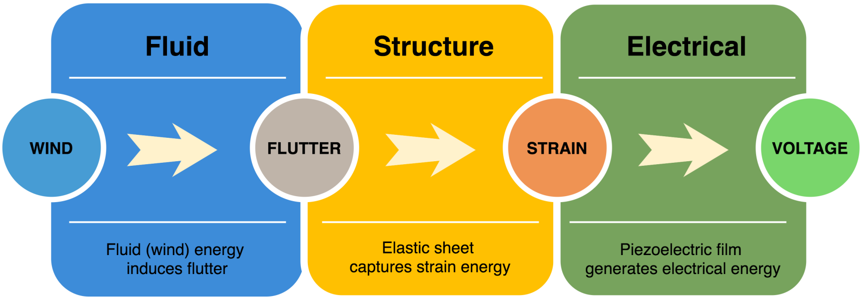

Figure 2.1: Energy harvesting strategy for the system where kinetic energy (of the fluid) is converted to strain, which is further converted to electrical energy.

### 2.1.1. Extraneously-Induced Excitation (EIE)

Extraneously Induced Excitation (EIE) is a type of flutter that was identified in [20, 21] that occurs when the immersed structure's excitation is caused due to external, time-varying flow pressure gradients, for instance, like those generated by a vortex shedding in the wake of a bluff body. Examples of this type of flutter include Vortex-Induced Vibrations (VIVs) and the flutter experienced by an aircraft wing near stall speed. Although for the purposes of wind energy harvesting, EIE flutter has been more widely employed than MIE flutter, it necessitates the need for a more complex setup and matching the dynamics of the flutter harvester to the upstream bluff-body vortex shedding. Moreover, the flutter phenomenon for EIE would not be suitable for a generic aircraft and UAV wind energy harvesting sensor and will be dependent on the geometry of the aircraft and will face a non deterministic time-averaged flow direction [18].

### 2.1.2. Movement-Induced Excitation (MIE)

Movement-Induced Excitation (MIE) is a type of self excited flutter that occurs due to the resonant bending instability of the immersed structure [20, 21]. At a certain flow velocity, usually termed as critical flutter speed, negative damping of the structure occurs which results in the divergence of structural deformations. This marks the onset of high amplitude oscillations in the immersed structure.

Seminal work by [22] used potential flow methods to prove that MIE flutter is a phenomenon that is self-excited and self-sustaining. [23] and [24] showed that there is a strong dependence of MIE flutter on the length and stiffness of the immersed structure. The orientation of the immersed compliant structure in the flow is a very important parameter that dictates the dynamics of the fluid structure interaction.

## 2.2. Inverted Flags and their dynamics

The immersed structure for this work consists of thin elastic piezoelectric films, which are placed in the wind flow. This allows for two distinct potential configurations: a regular flag and an inverted flag. An inverted flag is the mirror image of a regular flag with the leading edge left free to move, and the trailing edge is fixed. Fig. 2.2 shows the schematic of the inverted flag geometry for an elastic sheet. The sheet is shown using a solid straight line, and the curved dashed lines indicate the curvature of the film. $A$ denotes the maximum displacement between the tips in the $y$-axis, while $L$ and $W$ denote the length and width of the sheet, respectively. The inverted flag configuration for inducing flutter was first proposed by [25] and is motivated by the fact that any mechanical model with a free front and fixed rear end will be, in general, more susceptible to instability when faced with external axial loading than a regular flag. To explain, we can give a simple analogy of leaves fluttering in a breeze irrespective of their orientation to the wind, which justifies using this configuration as an alternative to the regular flag for flow-induced flapping.

There are three important parameters which are used to characterize the dynamics of interaction between a fluid flow and an inverted elastic film: bending stiffness $K_b$, aspect ratio $A_R$ and mass ratio $\mu$ [26–28]. They are calculated as,

$$\mu = \frac{\rho_s h}{\rho_f L} \tag{2.1}$$

$$A_R = \frac{W}{L} \tag{2.2}$$

$$K_b = \frac{Eh^3}{12\rho_f U^2 L^3 (1 - \nu^2)} \tag{2.3}$$

Here $\rho_s$ is the elastic sheet density, $\rho_f$ is the fluid density, $h$ is the thickness, $U$ is the free-stream velocity, $E$ is the Young's modulus, $\nu$ is the Poisson's ratio. $\mu$ represents the relative magnitude of structure to fluid inertial forces, while $K_b$ characterizes the relative magnitude of bending forces to the fluid inertial forces and can be used to classify three dynamical regime or modes for such a configuration:

1. *Straight mode* ($K_b > 0.3$): In this mode, the sheet remains straight. This regime exhibits behaviour analogous to fixed-point stability where after an initial disturbance, the sheet experiences positive damping and returns to a stretched-straight position.

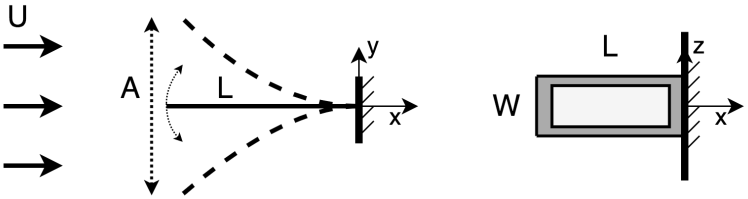

Figure 2.2: Inverted flag geometry of an elastic sheet. The solid (horizontal) line in the left image shows the sheet, and the dashed lines indicate curvature. The image on right shows the sheet dimensions.

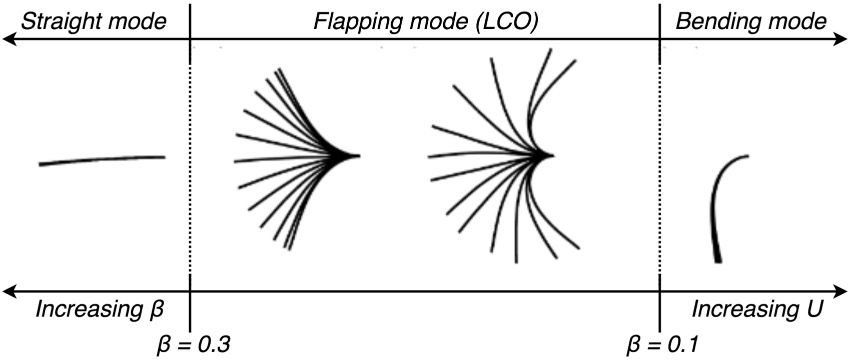

Figure 2.3: Illustration of the three modes of an inverted flag.

2. *Flapping mode* ($0.1 < K_b < 0.3$): In this mode, the sheet will flap from side to side and the deflection will be periodic. The magnitude of oscillations is the maximum in this mode.
3. *Deflected mode* ($K_b < 0.1$): In this mode, the sheet bends in one direction and maintains a highly curved or deformed shape.

The three modes are shown in Fig. 2.3.

## 2.3. Inverted flag: a critical design decision

The configuration used for developing Hermes is an inverted flag. The reasons for this choice which impacts the entire design and all the results obtained are multi-fold and described below:

1. **Higher energy harvesting**: The inverted flag shows greater peak-to-peak amplitude of deflection than the regular flag [25]. This means a greater magnitude of strain, which further implies a better potential for energy harvesting and sensing. The differences in the mean strain energy between an inverted flag and a regular flag were compared under the same flow characteristics and elastic properties in [29]. They found that the mean strain energy in the inverted flag was approximately 100 times greater than that in the typical regular flag. This implies that an inverted flag is more efficient in converting kinematic fluid energy into flag strain energy than the typical flag.
2. **Reliability**: The regular flag exhibits chaotic flapping beyond a critical bending stiffness while the inverted flag only experiences *limit cycle oscillations* within a specific range of $K_b$ [25]. Thus, an inverted flag exhibits higher stability and behaves more reliably than a regular one.
3. **Range**: In order to sense AoA and wind speed, it is essential that flutter can be induced over the typical operating range of wind conditions for any aircraft [30].

4. **Robust**: The accuracy of a regular flag is highly dependent on the wing/nose geometry, whereas the inverted flag is robust to it. The regular flag exhibits chaotic flapping beyond a critical bending stiffness while the inverted flag only experiences Limit Cycle Oscillations (LCOs) within a specific range of $K_b$ [25]. This has huge implications for flutter based sensing which will become largely unreliable in the chaotic flapping regime.

## 2.4. Piezoelectric harvesting: Picking a flexible film for flutter

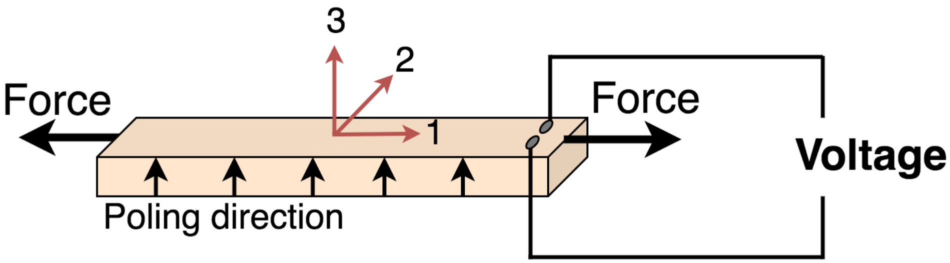

Figure 2.4: Schematic of -31 piezoelectric mode of operation for a $z$-axis poling direction PVDF sheet.

During flutter, piezoelectric films translate the induced strain into electrical energy. Piezoelectric material has one particular mode of operation that is relevant in our case: the $-[3\ 1]$ mode (see Fig. 2.4), which is affected by the piezoelectric constant $d_{31}$. Materials with high $d_{31}$ will generate more voltage and hence result in greater energy harvesting [18]. Another aspect of the piezoelectric material that is essential for flutter is the effective stiffness of the sheet, which must be controlled to excite flutter in the required wind speed ranges.

Although there are many different types of piezoelectric materials, there have generally been three piezoelectric materials used in the field of flutter harvesting, namely:

- Lead Zirconate Titanate (PZT)
- Macro-Fibre Composite (MFC)
- Polyvinylidene fluoride (PVDF)

### 2.4.1. PZT

PZT is a very common piezoelectric ceramic used for a wide variety of dynamic sensing applications [31]. Although it is classed technically as a ceramic, possessing a high stiffness makes it unsuitable for low-frequency applications such as flutter harvesters. Modern manufacturing techniques have allowed for PZT patches that are deployable in low-frequency energy harvesting applications[18] these patches are not widely available.

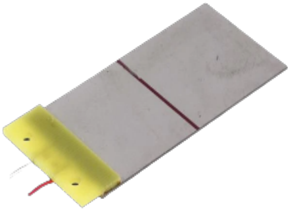

Figure 2.5: PZT Beam [1]

Figure 2.6: PVDF Film [2]

Figure 2.7: MFC Film[3]

### 2.4.2. MFC

MFCs or macro fibre composites are materials which generally comprise of precision engineered PZT fibres that are enclosed within adhesives, electrodes, and a layer of polyimide film [3]. MFCs are capable of relatively high power densities compared with other piezoelectric materials especially due to their high $d_{31}$ piezoelectric constants.

### 2.4.3. PVDF

Discovered in 1969, with having exhibited strong piezoelectric properties PVDFs are a popular choice for flutter harvesters. Their lower costs and greater availability have caused them to replaced PZT and MFCs in many sensory and battery applications as well [32]. PVDF undergo a poling process whereby the polymer is strained and placed within a strong electric or poling field. A great feature of PVDF films is that since PVDF is a polymer, it can be engineered to varied stiffness and toughness requirements which makes it versatile compared to PZTs and MFCs. The drawback is that PVDFs possess relatively low piezoelectric coefficients and a higher internal resistance and therefore by comparison, generally harvest an order of magnitude less power than an MFC of similar dimensions [18].

For flutter based harvesters though, since the harvester will flutter with large amplitude after the onset of critical airflow velocity, degradation or even permanent destruction of PZT patches and MFC might occur. Fracture and fragmentation occur often for fluttering PZTs while performance degradation and breakage can occur for MFCs [33]. PVDFs on the other hand, with their the high toughness, bear the ability to withstand large long term deformations.

## 2.5. Interplay between AoA and flutter

There have been numerous investigations about the effect of the AoA on the behaviour of an inverted flag under axial flow. In particular, the effect of the AoA on the transition between the different flapping states using a single polycarbonate plate has been investigated in [34]. It was found that at each of the angle tested (0° 10°, and 20°), the plate underwent a transition to large flapping. The experiment used stroboscopic imaging to show that there was a gradual growth of flapping amplitude when placed at an angle to the free flow stream. Additionally, it also showed that the nature of oscillations depend heavily on AoA.

This implies that there is sufficient scope to leverage the voltage information generated by piezoelectric film to infer AoA. Another recent study analyzes a polycarbonate plate in a wind tunnel to understand the effect of non-zero AoA on the dynamic response when placed in an inverted flag configuration under axial flow [35]. They performed experiments as well as 2D numerical simulations to show that the characteristic flow speeds, amplitudes, and frequencies vary with AoA. They also showed that large amplitude oscillations could exist for AoA up to 26.8°, which gives a large enough window for sensing. This further reinforces the idea that through analysis of the voltage generated by multiple geometries of piezoelectric films, one can indeed infer AoA while also harvesting energy.

# 3

# Controlled Wind Tunnel Experiments

With the necessary background, we now move to describing the various design aspects of Hermes using a controlled wind tunnel setup. We begin by characterizing the voltage response of the inverted piezoelectric flag for optimizing the sensing and energy harvesting performance. We study the effect of parameters such as dimension and orientation of the flags on the harvested energy and sensing. Let $\alpha$ and $U$ denote AoA and wind speed, respectively. The characterization was also used to develop an empirical model used for sensing.

## 3.1. Wind tunnel setup

Figure 3.1: Low speed wind tunnel used for controlled experimentation.

All these experiments were performed in a low speed open jet wind tunnel facility (Fig. 3.1) with a cross-section of 0.4 m × 0.4 m that could produce free-stream

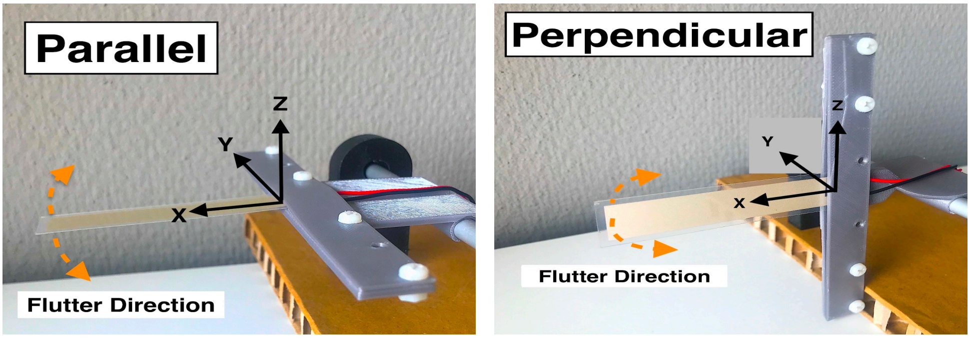

Figure 3.2: Two evaluated inverted piezoelectric flag orientations: parallel (in-plane) and perpendicular (out of plane).

velocities ($U$) between 0 and 30 m/s. It could be regulated by setting the revolutions per minute of the centrifugal fan. The wind tunnel had a large contraction ratio which kept the turbulence level of the flow in the test section to be low. Depending on the flow velocity, the minimum achievable turbulence level was in the order of 0.5%.

The wind speed was measured using an integrated pressure measurement system that used four-point pressure differential readings to estimate the wind velocity inside the test section. The accuracy of the wind velocity measurement is $\pm 0.10$ m/s. The piezoelectric flags were fastened in place using specially designed 3D printed clamps. We tested two different orientations of flags which differed in their plane of oscillations against the incoming wind. The two configurations are shown in Fig. 3.2 are parallel, where flapping is observed in the $z$ plane and perpendicular, where it is in the $x - y$ plane. Kapton tape is used to secure the flags firmly to the surface of the clamp. A specialized test rig was made to accurately change the orientation of the flag to the incoming wind and effectively set the angle of attack. The test rig comprised of a wooden base which was constructed from 20 mm plywood to fit into the test section of the wind tunnel. The base was smoothed and painted to ensure a smooth wind flow. On top of this wooden base an aluminum structure was created using 3D printed holders and 7 mm aluminum rods. Two NEMA 17 stepper motors were used to orient the flags in the $x - y$ and the $z$ direction, thereby setting the angle of sideslip and the angle of attack, respectively. The output of the inverted piezoelectric flag was measured by recording the output voltage from a single PVDF membrane, which was then used to calculate various signal features as well as the average generated power. All of the signals were recorded using a pre-calibrated Rocket Logger [36] capable of capturing voltage from 13 $\mu$V up to ±5.5 V. The voltage signal was sampled at 1 kHz for 5 s. A preamplifier from TE Connectivity, a Piezo Film Lab Amplifier, was used before sampling the output of the flag. The preamplifier was used to attenuate the output voltage of the flag, making it suitable for sampling and to varying the offered load resistance to the PVDF film. The motion of the inverted flags with different mass ratios is also captured using a

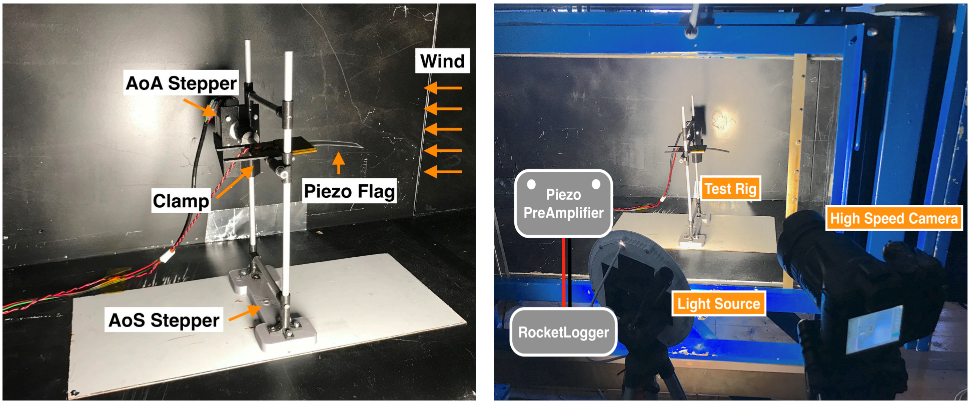

Figure 3.3: Constructed test rig and complete experimental setup.

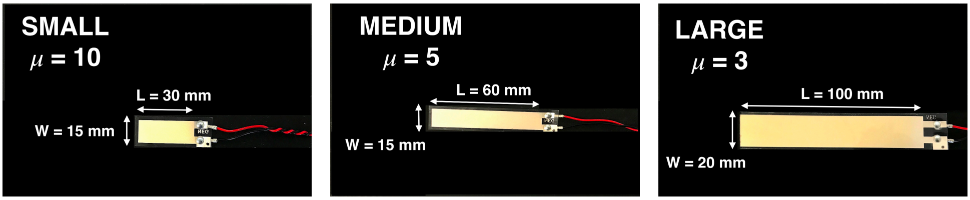

Figure 3.4: The three flags layouts labelled as Small, Medium and Large with their dimensions and mass ratios $\mu$ used in the wind tunnel study.

high-speed camera, High Speed EXILIM EX-F1. It is placed on a tripod in front of the test section and mounting it on top of the test section for parallel and perpendicular configurations, respectively. A dedicated 15W 80Ra light source illuminated the test setup placed laterally. The wind speed was increased incrementally, and videos were recorded at $600$ frames per second with a frame resolution of $432 \times 192$ pixels. These videos are used to measure the flapping frequency by calculating the time difference between images for a complete flapping oscillation.

The response of the inverted piezoelectric flag to the varying angle of attack was recorded by incrementally changing the angle from 0° up to 55° for each wind speed and for both of the flag orientations. Fig. 3.3 shows the constructed test rig, and the complete annotated wind tunnel setup is used to conduct the sensor study.

## 3.2. Design of piezoelectric flag

Piezoelectric flags made with different PVDF film dimensions are studied. Different designs comprised of widely available, commercial off the shelf, single poled piezoelectric films from TE Connectivity with a constant thickness of $t$ = 0.205 mm. These PVDF membranes were typically laminated with a 125 $\mu$m polyester layer to a 28 $\mu$m or 52 $\mu$m piezoelectric film element. These laminated films provide an inher-

Table 3.1: Piezoelectric PVDF films used for constructing different flag configurations.

| **Name** | **Part number** | **Length(L) (mm)** | **Width(W) (mm)** | **Thickness(t) (um)** | **Capacitance(C) (nF)** |
|---|---|---|---|---|---|
| LDT1-028K/L | 1-1002910-0 | 41 | 16 | 205 | 1.38 |
| LDT2-028K/L | 1-1003745-0 | 72 | 16 | 205 | 2.78 |
| LDT4-028K/L | 1-1002405-0 | 170 | 21 | 205 | 11.0 |

Table 3.2: Physical parameters of the three piezoelectric flags.

| **Physical Quantity** | **Value** | | |
|---|---|---|---|
| | **Small** | **Medium** | **Large** |
| PVDF film used | LDT1-028K/L | LDT2-028K/L | LDT4-028K/L |
| Length $L$ (mm) | 30 | 60 | 100 |
| Width $W$ (mm) | 15 | 15 | 20 |
| Thickness t (mm) | 0.205 | 0.205 | 0.205 |
| Aspect Ratio $A_R$ | 0.5 | 0.25 | 0.2 |
| Mass Ratio $\mu$ | 10 | 5 | 3 |
| Capacitance (nF) | 1.38 | 2.78 | 11.0 |
| Young's Modulus E (GPa) | 2.165 | 2.59 | 3.5 |
| Film Density $\rho_s$ (Kg/$m^3$) | 1780 | | |
| Poisson's Ratio $\nu$ | 0.34 | | |

ent structural rigidity when placed under flow thus, enabling their direct use as an inverted flag. Another reason is that when these films are used in a bending mode, the laminated film elements develop much higher voltage when flexed compared to non-laminated film elements. Additionally, the neutral axis of the film is in the laminate rather than in the film which results in the film getting strained more when flexed and causing less charge cancellation [37]. The three types of films were used to prepare three flags with widths $W = 15$ mm, 15 mm and 20 mm and lengths $L = 30$ mm, 60 mm and 100 mm respectively. The resulting flags called small, medium and large had mass ratio $\mu = 10$, 5 and 3 and an aspect ratio $A_R = 0.5$, 0.25 and 0.2, respectively. The three flags are shown in Fig. 3.4.

Certain physical specifications of the flag were needed to calculate the different non-dimensional parameters which ultimately govern the response of the inverted flags. These quantities are summarized in Table 3.2. The Young's modulus of the flag used to estimate its bending stiffness $K_b$ in particular, had to be experimentally determined using a quasi-static tensile test. We found that the value of Young's modulus for all three films are between $2 - 4$ GPa in accordance with the manufacturer. Other physical parameters like Poisson's ratio $\nu$ and density of the membrane $\rho_s$ are based on the datasheet and previous experimental work [30, 37].

The effect of $A_R$ on the energy harvesting potential was also evaluated for two

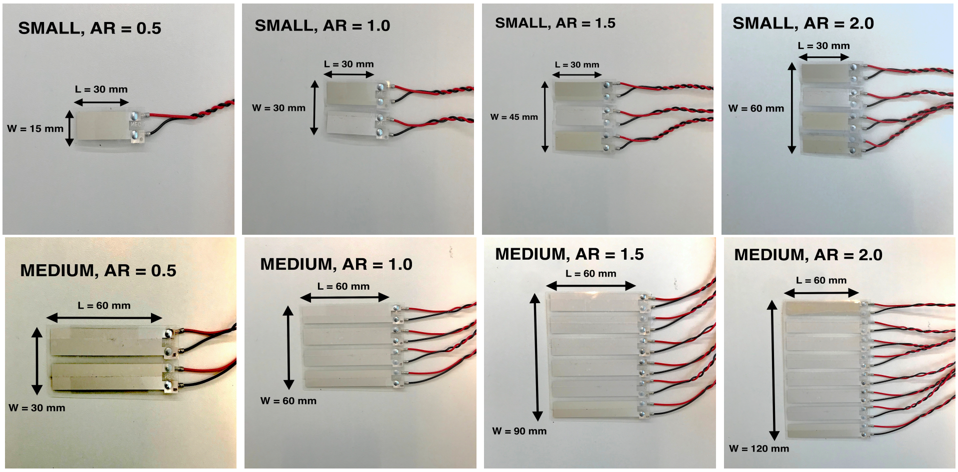

Figure 3.5: Flags with aspect ratios, $A_R$, from 0.5 to 2.0 for PVDF films with $\mu = 10$ and $\mu = 5$.

of the flags – small, $\mu = 10$ and medium, $\mu = 5$. The $A_R$ was varied from 0.5 to 2.0 with increments of 0.5 to create four additional flags for each of the two mass ratios creating eight additional flags shown in Fig. 3.5. The flags were prepared by stacking multiple appropriate PVDF films till the required width of the flag was obtained.

### 3.2.1. Auxiliary Note

We contacted the principal investigator in [30] to confer about the usage of aluminum rods as a mounting mechanism. The author admitted that indeed there is a problem in using rods and the using clamps can alter the flutter characteristics. Since using aluminum or similar rods for mounting the flags was neither practical nor possible on a test rig with changing Angle of Attack, we decided to use a 3D printed clamp design. We also discussed with the author about the exact methodology followed to create flags with different Aspect Ratio by stacking multiple PVDF films since this was not made apparent from their journal paper. The authors were kind enough to answer our questions about the process and ultimately helped us decide on the exact construction process for the flags shown in Fig. 3.5

# 4

# Characterization of Inverted Flag

We now characterize the energy harvesting and sensing capability of the piezoelectric films through controlled experimentation.

## 4.1. Identification of three flapping regimes

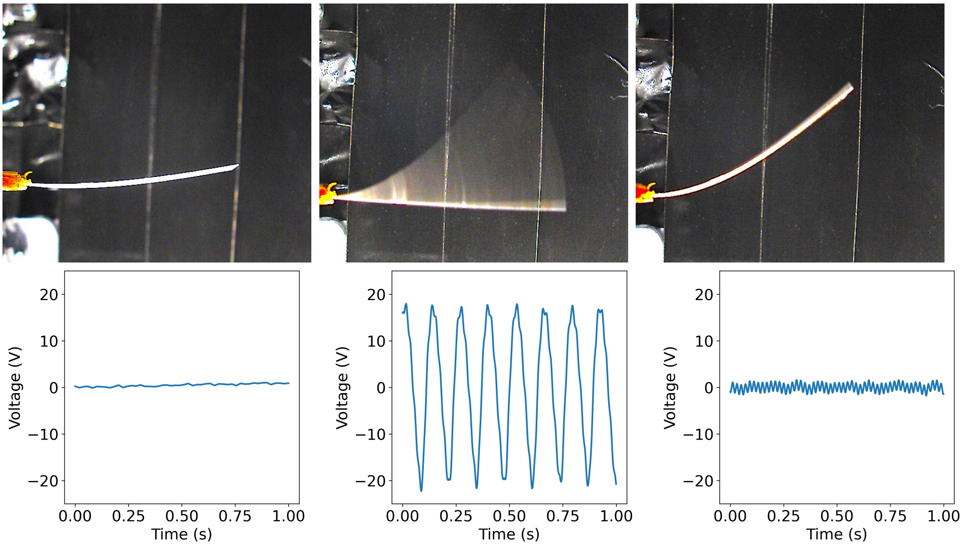

Figure 4.1: Three flapping regimes for piezoelectric flag and corresponding voltage signals.

We observed the three regimes of flutter governed by the value of bending stiffness $K_b$. The flapping regimes and the generated voltage waveform for a mediumsized flag in the perpendicular configuration are shown in Fig. 4.1. We observed flutter for $K_b$ = 0.1 to 0.3 [25, 30]. We did, however, observe asymmetrical oscillations for both the parallel and perpendicular. This can be attributed to the different styles of mounting clamp we used compared to other similar experiments where the films were mounted on an aluminum rod [30].

## 4.2. Selection of Optimal Load Resistance

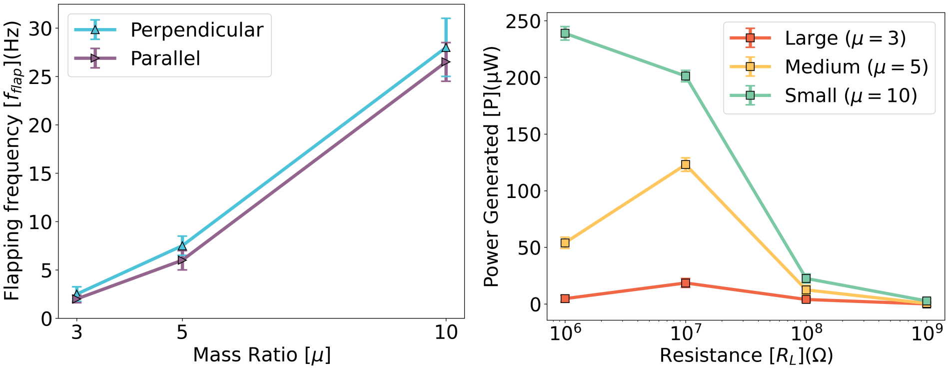

Figure 4.2: Selection of $R_{\mathrm{OPT}}$ by determination of flag flapping frequency and harvested energy with varying load resistances.

To harvest maximum energy, it was necessary to select an optimal value of load resistance, $R_{\mathrm{OPT}}$ which depends on the flapping frequency and film capacitance and can be calculated as $R_{\mathrm{OPT}} = 1/2\pi f C_f$, where $f$ and $C_f$ are the flapping frequency and capacitance of the film, respectively [38]. The videos recorded from the high speed camera were used to estimate the flapping frequency for all three flags as shown in Fig. 4.2 along with the harvested energy with varying load resistance connected to each flag in the perpendicular configuration. The results are shown for $K_b = 0.1$ where the harvested energy is maximum. The error bars depict standard deviation for 5 measurements. The trend shows that flags with mass ratio $\mu$ of 5 and 3 harvest maximum energy at 10 M while the heavier flag with $\mu = 10$ harvests more energy at 1 MΩ.

## 4.3. Energy harvesting performance

The energy harvesting potential and energy density of different flags were characterized by observing the generated power. This was calculated by using the load resistance $R_L$ and RMS value of the generated voltage. The peak voltage was found for every 100 samples and averaged over 1 s and then used to calculate the RMS voltage.

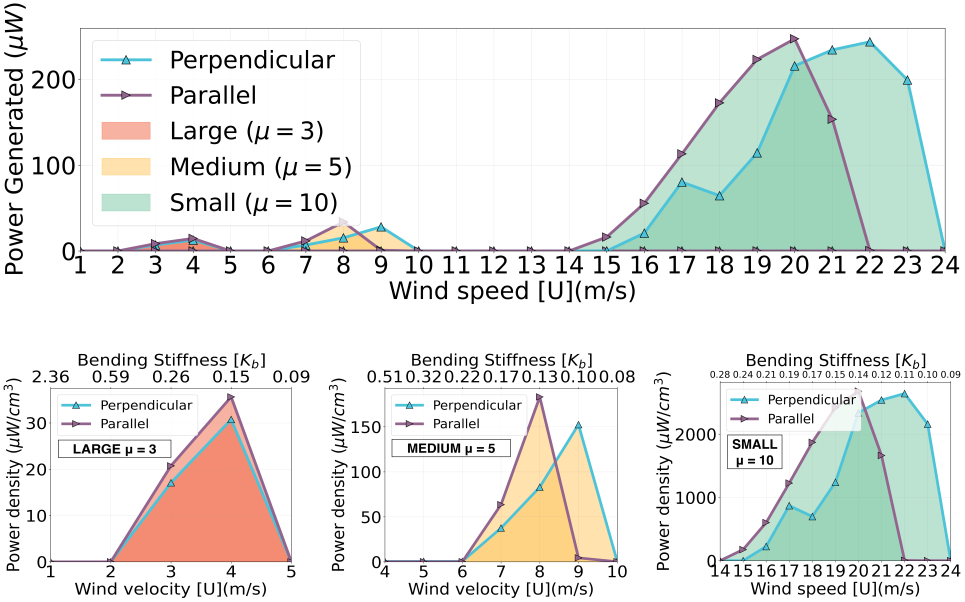

Figure 4.3: Evaluation of harvested energy by all flags for $\alpha = 0$ (top) and interpreting the power density variations with bending stiffness for $\mu = 3$, $\mu = 5$ and $\mu = 10$.

### 4.3.1. Effect of Mass Ratio

Fig. 4.3 shows the effect of the mass ratio of the flags on the harvested power over varying wind speeds. All three flags experienced flutter over different wind speed ranges. It can be seen that for small aspect ratio ($A_R < 1$), the small flag with $\mu = 10$ generates the largest power. The large flag had a smaller wind speed range and did not possess a very high power density for $A_R = 0.2$ and was thus found to be unsuitable for our sensor. The figure also shows the power densities for small and medium flags interpreting them in the context of $K_b$. Both flags show flutter between $K_b = [0.1, 0.3]$ with the maximum power density for the $K_b = 0.1$ case. Interestingly, the range of wind speed where flutter occurs diminishes slightly for the parallel configuration compared to the perpendicular one. This can be explained by the effect of gravity on the oscillatory motion resulting in lower stability of flag.

### 4.3.2. Effect of Aspect Ratio

Since power density of the inverted flags is susceptible not only to the mass ratio but also to the aspect ratio of the flags, experiments were carried out with eight additional flags with varying dimension as stated in Section 3. Fig. 4.4 shows the resulting power generated with varying aspect ratio for given wind speed and bending stiffness for flags for $\mu = 5$ and $10$. The power generated increased considerably with the increase in aspect ratio owing in part to the additional PVDF films and partly due to increased flapping amplitude which can be inferred from the increased peak voltage. This result can also be verified in [30].

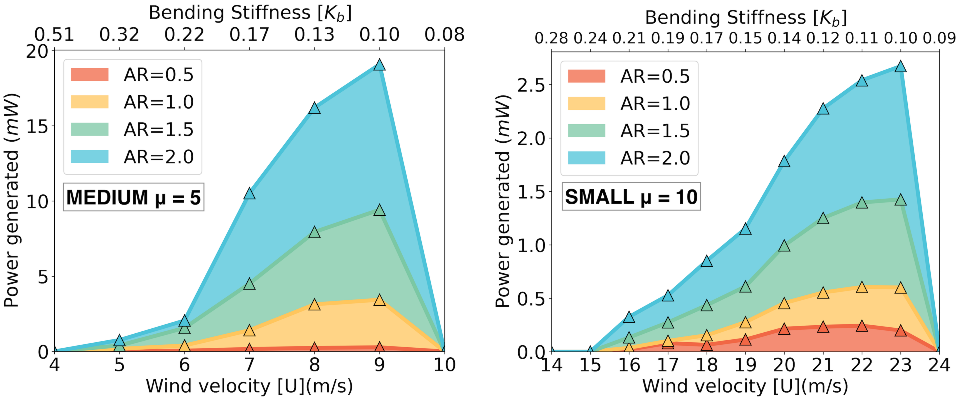

Figure 4.4: Evaluation in energy harvested with varying $A_R$ for $\mu = 5$ (left) and $\mu = 10$ (right) for different speeds with $\alpha = 0$.

### 4.3.3. Effect of Angle of Attack

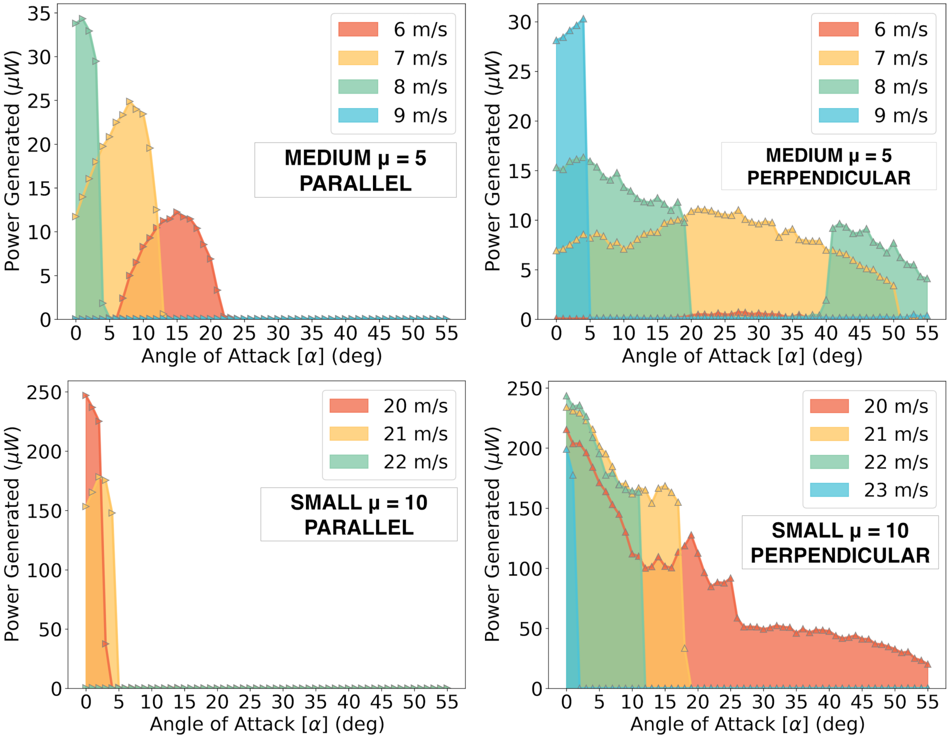

Figure 4.5: Evaluation in harvested energy for different $\alpha$ and $U$, and flag orientations.

Finally, the range of AoA and wind speed for effective energy harvested can be discerned from Fig. 4.5. Clearly, the small flag shows a usable range of energy generation over the entire AoA range from 0°to 55°for $K_b \in [0.1, 0.15]$, justifying our choice of small flag in the perpendicular configuration.

## 4.4. Voltage features for sensing

Here, we analyzed the voltage generated by the piezoelectric flag for two features for sensing wind speed and AoA: (a) peak voltage ($V_p$) and (b) zero crossing frequency ($f_z$). $V_p$ matches with the peak amplitude of flapping, while $f_z$ relates to the flapping frequency. These two features thus represent the flutter characteristic in the electrical domain.

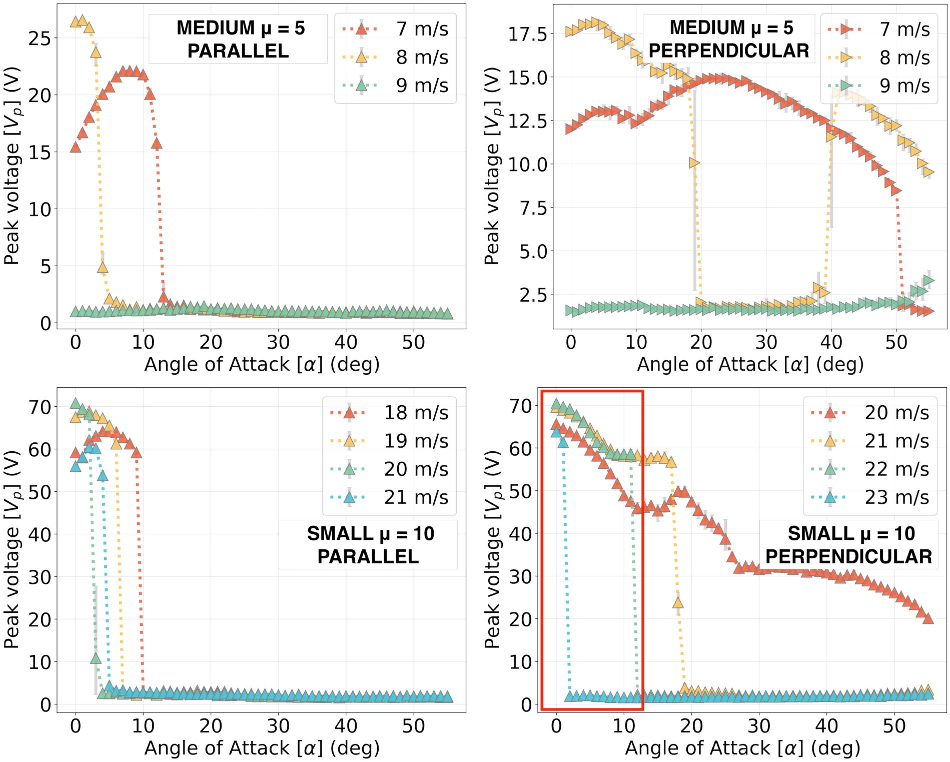

Figure 4.6: Evaluation of peak voltage variation obtained for different $\alpha$, $U$, and flag orientation.

Figs. 4.6 and 4.7 show the trends observed for these two features for different $\alpha$, $U$ and flag orientations. The graphs are plotted for the mean value from 5 separate trials with a trial duration of 5 s. $V_p$ is calculated over every 100 samples and averaged over 500 ms. $f_z$ is calculated over 500 ms intervals. The wind speed ranges considered directly follows from the energy harvesting performance of each flag across the ranges of $U$ and $\alpha$. It was found that for both mass ratios, the perpendicular configuration showed a more uniform decaying trend of $V_p$ with $\alpha$.

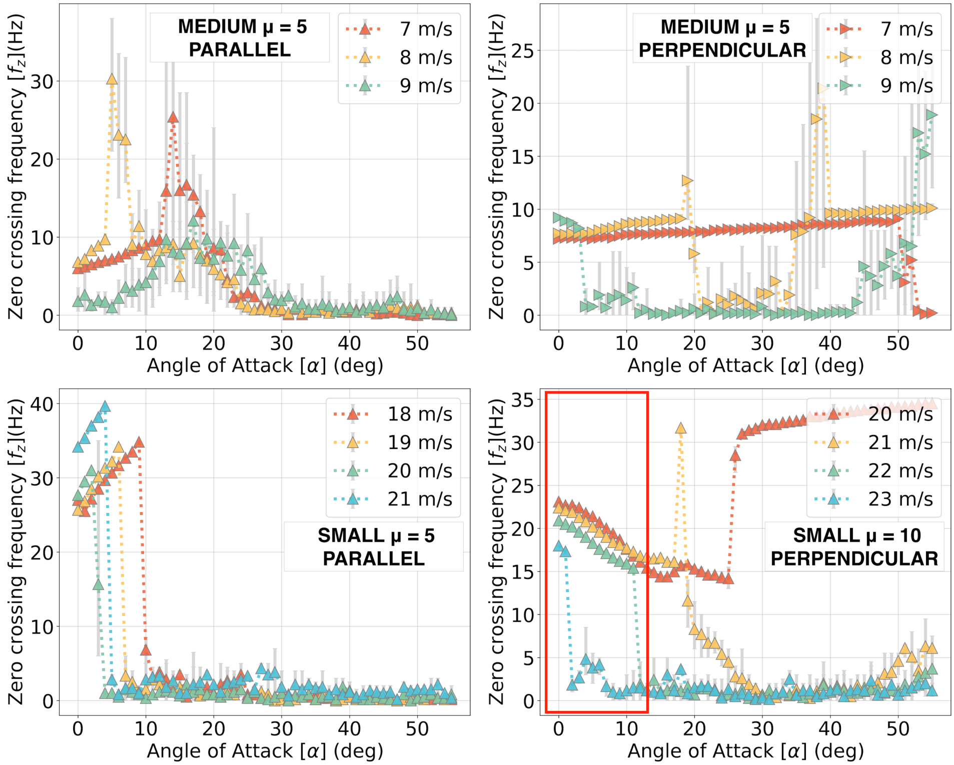

Figure 4.7: Evaluation of zero crossing frequency variation for different $\alpha$, $U$ and flag orientation.

However for certain ranges of $\alpha \in [15°, 25°]$ for $\mu$=5 and $\alpha \in [10°, 30°]$ for $\mu$=10, the perpendicular flags showed a peak which could be attributed to the flag being exposed to a cross-flow component that induces flutter. The flags oriented in parallel do not show this phenomenon as expected from their orientation. At $\alpha$>10°, these flags remain in the bent mode and do not show any significant flapping. The perpendicularly oriented flags are less affected by changing $\alpha$. All flags show increased sensitivity to changes in $\alpha$ at higher $E$ as expected. The high variability in the observed $f_z$ at $\alpha$ >10° is due to low amplitude flapping of the flags at these angles.

Fig. 4.6 confirms that the oscillations are not large, and the flags are in the bent mode. Even in that mode, these low amplitude flutter oscillations still created high frequency components in the flags. The variation in frequency for the small flag in perpendicular configuration shows its potential for carrying information regarding $\alpha$ and $U$ in the range $\alpha \in [0°, 10°]$. From these results, it is evident that only the small flag in the perpendicular configuration shows an invertible relationship between $(\alpha, U)$ and $(V_p, f_z)$. This cements the decision for the use of the small flag as the sensing element.

# 5

# Design of Hermes

In this section, we present the various design details of Hermes.

## 5.1. System Design

Based on the controlled experiments and insights gained from Section 3, we carry out the design of the proposed system. Hermes harvests energy from wind flow and uses it to drives specifically built miniature microcontroller board to find $\alpha$ and $E$. It transmits the measurements over a wireless link. This section delineates the sensor system design. Fig. 5.1 shows the functional block diagram of Hermes. The system consists of three functional blocks: piezoelectric flag, energy conditioning, and the microcontroller and sensing blocks.

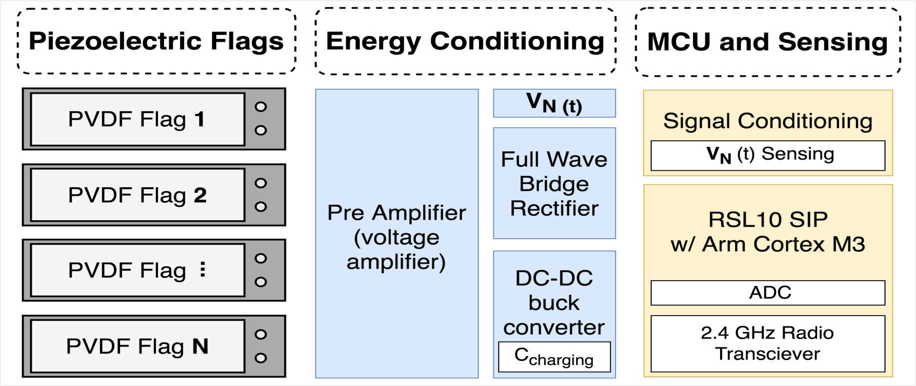

Figure 5.1: Functional block diagram representation of Hermes.

### 5.1.1. Piezoelectric flag:

This block consists of an array of five single poled PVDF piezoelectric films ($L$ = 30 mm, $W$ = 15 mm and $\mu = 10$) which are used as inverted flags oriented in the perpendicular configuration (direction of flutter in $x - y$ plane). These flags form both the sensing as well as the harvesting element. Each of the flags is mounted at an angle of 10° from the other. Fig. 5.2 shows the fabricated Hermes PCB with all system blocks along with the mechanical mount design. The flags are held in place using specially designed rigid clamps that orient the flags at the required mount angle. Each flag, based on the incoming wind direction, will exhibit prominent flapping in a range of [0, 10]° from the central axis of the flag. Together, at least one of these five flags will flutter within a 40° range in wind direction. The generated voltage from each flag is fed to the energy conditioning block for harvesting and sensing.

### 5.1.2. Energy conditioning:

The output of each flag, $V_N(t),\ 1 \leq N \leq 5$ is fed to a preamplifier, which is used as a voltage amplifier for the piezoelectric films [39] and function as a buffer between the piezoelectric films and the rest of the circuit. The preamplifier is able to provide the required load resistance $R_{\mathrm{OPT}}$ as seen by the flags. This value for the small flags was found to be between 1 MΩ and 5 MΩ for different flapping frequencies, and thus, a median value of 3.3 MΩ was chosen; the discussion is omitted for paucity of space. The preamplifier output is fed to the signal conditioning circuit before being sampled by the ADC in microcontroller and to the power harvesting and rectifying circuit for powering the sensor as well. We use LTC3588, a full-wave bridge rectifier integrated with a high-efficiency buck converter for the purpose of rectifying and stepping down the generated piezo voltage due to its extremely low-power consumption and small footprint. The output of the buck converter is directly used to power the microcontroller.

### 5.1.3. Micro controller and sensing:

The signal $V_N(t)$ needs to be conditioned to make it possible for the ADC to sample it. This is done by using a resistive voltage divider circuit for scaling, which maps the generated voltage between 0 to 2 V. High impedance resistors are used to minimize current. The negative swing of the voltage waveform is inverted using an ultra low-power OpAmp, MAX44264, that provides the inverted value to the voltage scaling section and is then fed to the microcontroller.

We use ON Semiconductor’s RSL10 System−In−Package (RSL10 SIP), which contains an integrated on-board antenna, BLE radio SoC and all necessary passive components in a single package. It is ultra-low power and has a highly flexible multi-protocol 2.4GHz radio. Using this chip, the entire sensor design requires 360 $\mu$J to communicate at 6 dBm maximum transmit power. The ADC in RSL10 can record voltage between 0 to 2 V, and can sequentially sample 8 channels at a maximum sampling rate of 6.25 kHz with a resolution of 14 bits. We use it to sample the $V_N(t)$ signal after it is passed through the signal conditioning block,

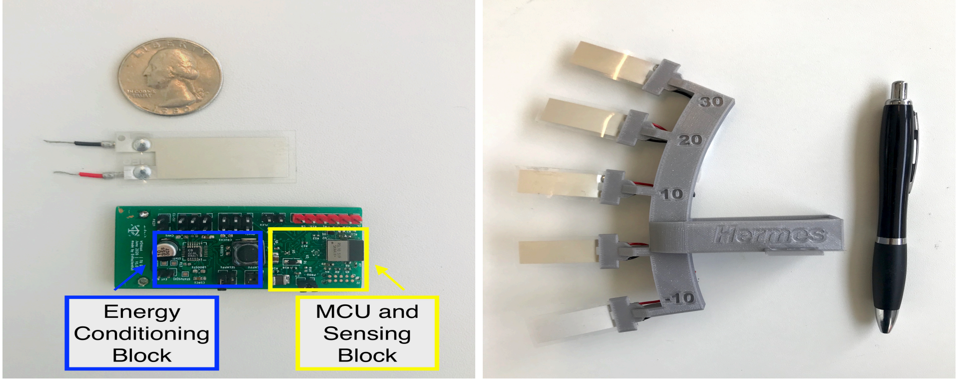

Figure 5.2: Fabricated Hermes Printed Circuit Board (PCB) and 3D printed sensor mount.

making it compatible with the SIP's ADC. The signal is recorded for each of the piezoelectric flags at 1 kHz sampling rate for 500 ms. This signal is then fed into the real-time algorithm (discussed in Section 5.2) for estimation of $\alpha$ and $U$. Once that is calculated, the SIP transmits the measured quantities as BLE beacons using one of the three advertising channels. Since the sensor is self-powered, there is no scope for a connection oriented mechanism. Hermes powers on with the incoming wind, which induces flutter of the piezoelectric flags resulting in powering of the sensing circuit. In the current design, the sensor continuously broadcasts sensed data at a rate of 2 Hz in the presence of wind. Different communication protocols can be implemented on Hermes, the details of which we omit here. The sensor is mounted at the tip of the airfoil of the aircraft. Since the sensor faces the incoming wind without a bluff body, wake effects can be ignored if the sensor is mounted sufficiently far away from the fuselage. The mount can be manufactured using the requisite material based on wind speed and end application considerations, e.g., carbon-fiber. The volumetric size of the mount and sensors is $27.5\,cm^3$ and the weight of the flags and sensor PCB without the mount is about 60 g.

## 5.2. NSR Algorithm for estimating AoA, wind speed

We propose *Nonlinear Surface Regression* (NSR) – an estimation algorithm which uses the generated voltage signals from the piezoelectric flag array to dynamically estimate the AoA and wind speed from the incoming airflow. The algorithm comprises of three stages: i) *Nonlinear surface generation*, ii) *AoA range separation*, and iii) *Iterative nonlinear inversion*. Stage i) is performed once, offline, during calibration, while ii) and iii) are performed online in the respective sequence.

### 5.2.1. Stage 1: Nonlinear surface generation

From the voltage signal $V_N(t)$ of each piezoelectric flag, where $1 \leq N \leq 5$, the peak voltage $V_{pN}$ and zero-crossing frequency $f_{zN}$ have been averaged over 500 ms of data, generating time-series $V_{pN}(t_k)$ and $f_{zN}(t_k)$ sampled at 0.5 Hz. From Figs. 4.6

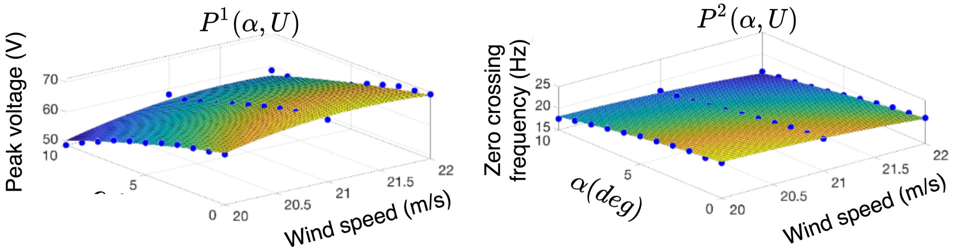

Figure 5.3: Surface polynomials for expressing $V_{pN}$ and $f_z$ as functions of $\alpha$ and $U$.

and 4.7, it can be seen that $V_{pN}$ and $f_{zN}$ exhibit a monotonic trend when $\alpha \in [0, 10]°$ and $U \in [20, 22]$ m/s for the small perpendicularly oriented piezoelectric flag. Therefore, using the data points in Fig. 4.6 and Fig. 4.7, an empirical nonlinear relation has been derived as $V_{pN} = P^1(\alpha, U)$, $f_{zN} = P^2(\alpha, U)$, where

$$P^i(\alpha, U) = \sum_{j=0}^{2} \sum_{k=0}^{2} P^i_{j,k} U^j \alpha^k. \tag{5.1}$$

The coefficients $P^i_{j,k}$, have been determined using a *robust linear least squares* algorithm. The coefficients have been determined with $95\%$ confidence, and given in Table 5.1, and the corresponding surface polynomials have been shown in Fig. 5.3. From the above coefficients, we determine that

Table 5.1: Coefficients of surface polynomials

| i | $P^i_{0,0}$ | $P^i_{1,0}$ | $P^i_{0,1}$ | $P^i_{2,0}$ | $P^i_{1,1}$ | $P^i_{0,2}$ |
|---|---|---|---|---|---|---|
| 1 | -1152.4 | 114.5 | -3.6 | -2.7 | 0.1193 | 0.0351 |
| 2 | -162.7 | 18.94 | -0.3782 | -0.4818 | -0.0004545 | -0.0141 |

$$\operatorname{rank} \frac{\partial(P^1, P^2)}{\partial(\alpha, U)} = 2, \; 0 \le \alpha \le 10, 20 \le U \le 22 \tag{5.2}$$

and therefore from the inverse function theorem, we deduce that the relation $(V_{pN}, f_{zN}) = \big(P^1(U, \alpha), P^2(U, \alpha)\big)$ is invertible, allowing us to determine $\alpha, U$ from $V_{pN}, f_{zN}$ as long as $0 \le \alpha \le 10°$. Note that since the trend for $V_{pN}$ and $f_{zN}$ is independent of the sign of $\alpha$, we only obtain $|\alpha|$ for negative AoA using the surface polynomials.

### 5.2.2. Stage 2: Determining AoA range

From the structure of Hermes (Fig. 1.1), notice that when the $\alpha \in [-10°, 30°]$, at least one of the five piezo flags is within an angular separation of $10°$ from the wind velocity vector $\vec{U}$, as illustrated in Fig. 5.4. Since the nonlinear surface regression

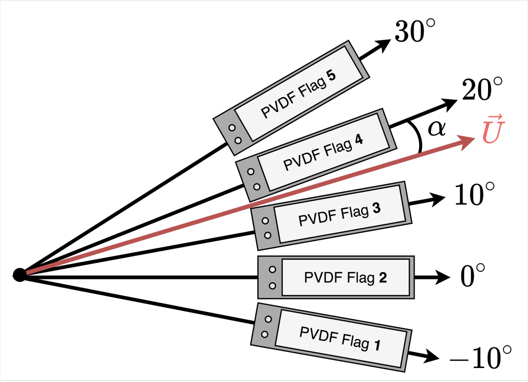

Figure 5.4: Schematic of piezoelectric flag array for sensing a wide range of AoA

is only applicable when $\alpha$ is within $\pm 10°$, it is necessary to determine the piezo flag which is within this range, and which makes a minimal angle with $\vec{U}$. Further, since the surface regression only gives us the absolute value of the angular separation, it is necessary to determine the sign of the angular separation as well. The above is achieved via Algorithm 1.

**Algorithm 1:** AoA range detection algorithm

```
Result: Determine:
    1. $N$ such that the $N^{th}$ piezo makes minimal angle $\alpha_N$ with $\vec{U}$,
    2. $\mathrm{sign}\ (\alpha_N)$
Set $N = \min\left(\arg\max_{1 \le i \le 5}(V_{pN})\right)$
if $1 < N < 5$ then
    if $V_{pN+1} < V_{pN-1}$ then
        $\mathrm{sign}\ (\alpha_N) > 0$
    else
        $\mathrm{sign}\ (\alpha_N) < 0$
else
    if $N = 5$ then
        $\mathrm{sign}\ (\alpha_N) < 0$
    else
        $\mathrm{sign}\ (\alpha_N) > 0$
end
```

The algorithm is based on the fact that, in case of the small-size piezo flag in a perpendicular orientation (as seen in the fourth quadrant of Fig. 4.6), the flag which makes a minimal angle with the wind velocity vector also generates the largest $V_p$. This is because, as seen in Fig. 5.4, if one of the piezo flags makes a minimal absolute angle $\alpha$, then all other piezo flags make an absolute angle which is in the set $\{10i \pm \alpha,\ 1 \leq i \leq 4\}$, and it can be observed that $V_p(\alpha, U) > V_p(10i \pm \alpha, U),\ 1 \leq i \leq 4$.

### 5.2.3. Stage 3: Iterative nonlinear inversion

Having determined $n$ and $\operatorname{sign}(\alpha_n)$ in the previous step, we now describe an iterative algorithm for determining $|\alpha_N|$, based on Newton-Raphson method. From (5.2), there exists an inverse relation $(|\alpha_N|, U) = P^{-1}(V_{pN}, f_z)$, where $P^{-1}$ is computed iteratively via Algorithm 2.

**Algorithm 2:** Iterative nonlinear inversion for AoA, wind speed

```
  Result: Determine $(\alpha, U)$ given $(V_{pN}, f_{zN})$
1 Obtain $N$ and $\operatorname{sign}(\alpha_N)$ from Algorithm 1; Set $[\bar{\alpha}_N, \bar{U}]$ as a nominal point
    close to the range in which we estimate $|\alpha_N|, U$ ;
2 Set
    $\begin{bmatrix} \bar{\alpha}_N^+ \\ \bar{U}^+ \end{bmatrix} = \begin{bmatrix} \bar{\alpha}_N \\ \bar{U} \end{bmatrix} - \gamma \left[ \frac{\partial (P^1, P^2)}{\partial (\bar{\alpha}_N, \bar{U})} \right]^{-1} \begin{bmatrix} P^1(\bar{\alpha}_N, \bar{U}) - V_{pN} \\ P^2(\bar{\alpha}_N, \bar{U}) - f_{zN} \end{bmatrix},$
3 if $(\bar{\alpha}_N - \bar{\alpha}_N^+)^2 + (\bar{U} - \bar{U}^+)^2 < tol$ then
4     $|\alpha_N| = \bar{\alpha}_N^+, U = \bar{U}^+$, go to step 7
5 else
6     Set $\bar{\alpha}_N = \bar{\alpha}_N^+, \bar{U} = \bar{U}^+$, go to step 2
7 AoA: $\alpha = 10(N-2) + |\alpha_N| \operatorname{sign}(\alpha_N)$.
```

Here $\gamma$ is the step size of the iterations and $tol$ is the error bound. For our implementation we set $tol = 0.01$ and $\gamma = 0.5$.

# 6

# Performance Evaluation

With all the necessary building blocks of Hermes in place, we now perform its comprehensive evaluation. We begin by presenting its sensing accuracy in the controlled wind tunnel setup followed by realistic evaluations over a wireless communication link inside a Boeing 737 fuselage.

## 6.1. Sensing accuracy and harvesting

We study the performance of NSR algorithm in the wind tunnel setting over a wide range of $\alpha \in [-10°, 30°]$ and $U \in [20,\ 22]$ m/s. Fig. 6.1 shows the comparison between actual and estimated values of $\alpha$ and $U$. Although it is hard to track extremely minor variations in $U$ (which in reality is unnecessary), averaging provides

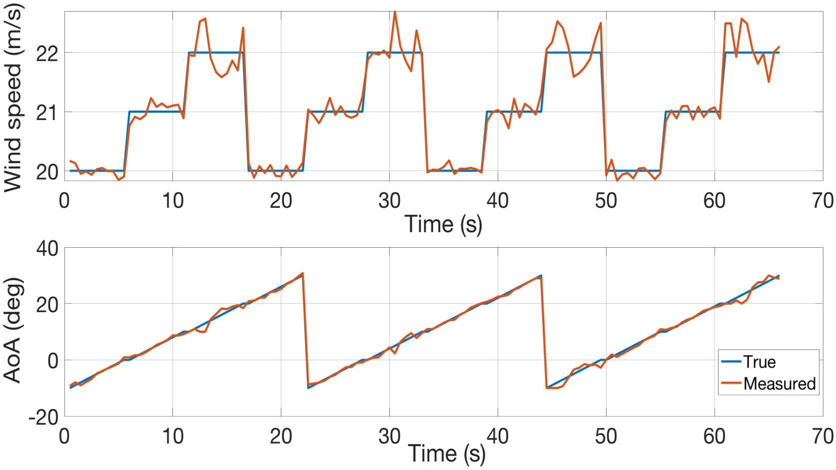

Figure 6.1: Comparison between actual and estimated wind speed and AoA.

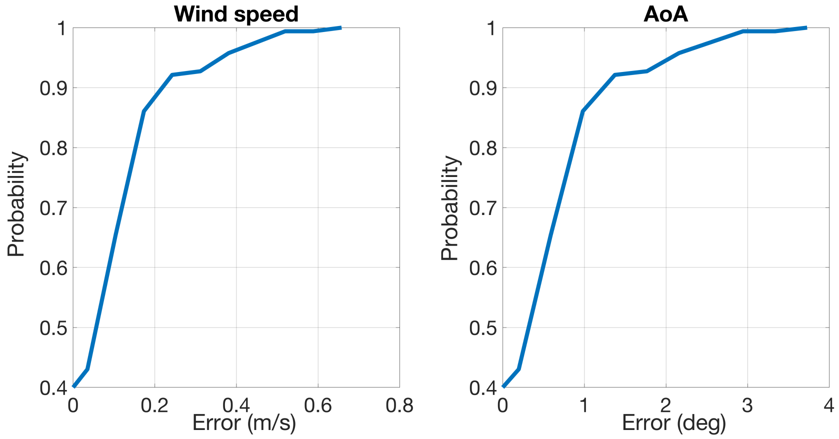

Figure 6.2: CDF of error in $U, \alpha$ corresponding to Fig. 6.1

considerable accuracy. On the other hand, it can be seen that the accuracy of $\alpha$ is significant, substantiating the high performance of Hermes. In Fig. 6.2, we plot the CDF of estimation errors. While the estimation error of $U$ is below 0.2 m/s with 90% probability, the error of $\alpha$ is within $1.2°$ with $90\%$ probability and within $2°$ with $95\%$ probability. For the chosen averaging interval (for $V_p$ and $f_z$) and the parameters of the Newton algorithm, the sensing rate is 2 Hz. Note that the sensing accuracy by reducing the tolerance, error bound, and averaging interval, albeit at the cost of a lower sensing rate. Further, one can also improve the sensing accuracy by choosing higher degree surface polynomials. Fig. 6.3 shows the energy harvested by Hermes over the entire range of $\alpha$. It can be seen that Hermes can harvest at least 377 $\mu$W and a mean of 440 $\mu$W over the considered range of $\alpha$. Note that energy harvested

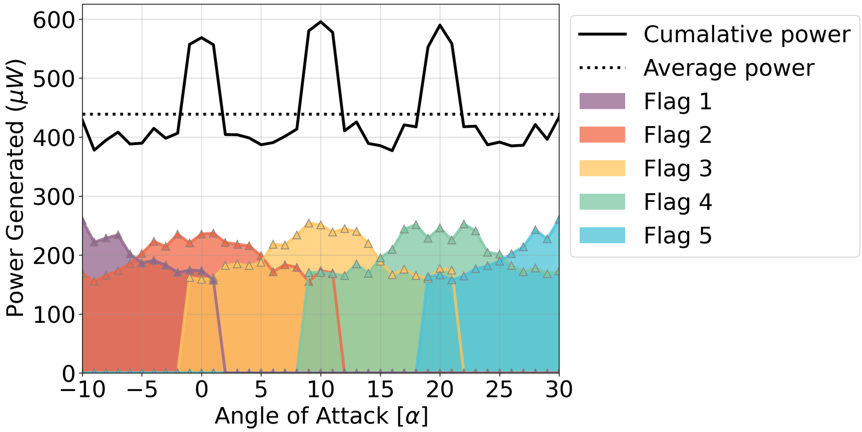

Figure 6.3: Energy harvested by the sensor over entire operational range by different flags.

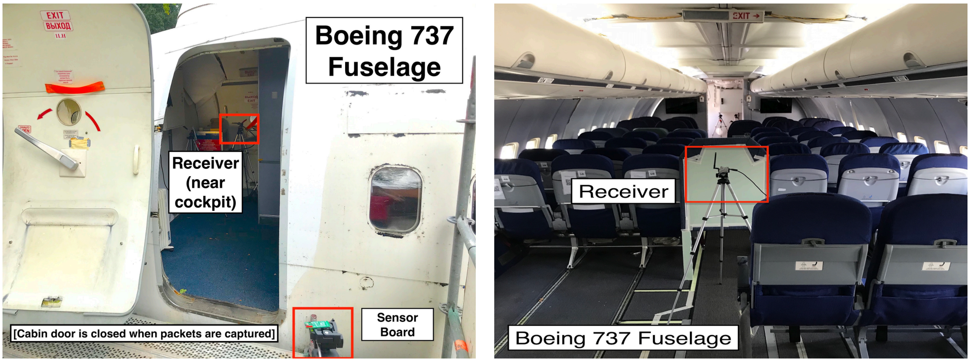

Figure 6.4: Sensor wireless signal transmission experimental setup inside a Boeing 737 fuselage.

from multiple films can be utilized simultaneously, unlike AoA which is drawn from only one film. This power is sufficient for transmitting the sensed value at 2 Hz at low power (0 dBm and lower) and at 1 Hz for max power (6 dBm).

## 6.2. Wireless communication

### 6.2.1. Experimental setup

We now move to conducting measurements inside an actual fuselage of Boeing 737. Since it is infeasible to mount Hermes on a flight in operation, the best we can do is to measure its performance under realistic wireless signal attenuation and propagation conditions.

This environment replicated, to a large degree, the wireless conditions encountered by a sensor mounted on an airplane wing. Fig. 6.4 shows the test setup inside the fuselage. Since the wind energy inside the fuselage is not sufficient for energy harvesting, we power Hermes using a coin cell 3V battery.

### 6.2.2. Findings

We conduct several measurements by varying the distance between Hermes and BLE receiver as well as the transmission power. In addition to the fuselage experiments, the power consumption of Hermes was evaluated for different data transmission rates and transmission powers to experimentally determine its energy budget.

Fig. 6.4 shows the evaluation setup inside the fuselage. We broadcast BLE advertising packets of size 40 bytes at 2 Hz to simulate the sensor transmission characteristics. We vary the distance between Hermes and BLE receiver from 1 m to 5 m and transmission power from 6 dBm to -6 dBm. The justification for restricting the distance is the following: Typically, AoA and wind speed sensors are mounted close to the nose and not very far from the wing to get unobstructed airflow, and this distance does not exceed 5 m.

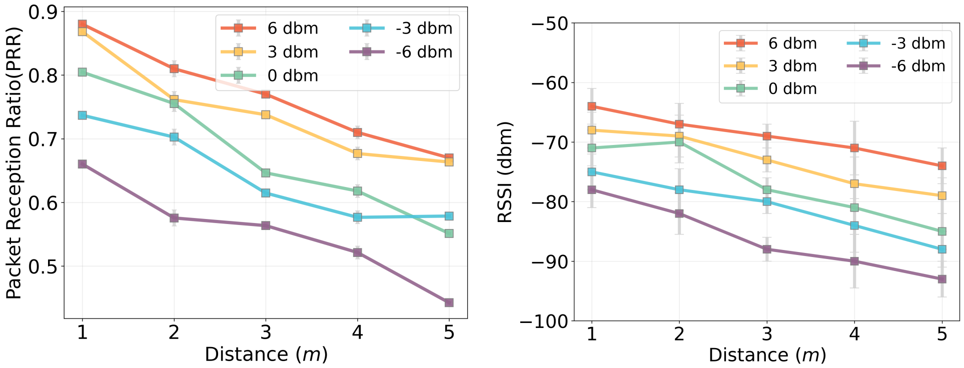

Figure 6.5: Packet reception ratio (PRR) and RSSI of for varying distance and transmission power.

Fig. 6.5 shows the variation of Packet Reception Ratio (PRR) and RSSI measured over a duration of 500 s. It can be seen that Hermes can achieve a maximum PRR of 89% at transmission power of 3 dBm and 6 dBm, and a maximum RSSI of -63 dBm at 6 dBm power. This shows that a reasonably reliable communication is achieved.

In order to further the research of wireless signal characterization using different communication standards, we plan to provide RSSI data from our fuselage experiments publicly.

## 6.3. Hermes form factor and adaptability

Table 6.1: Form factor evaluation metrics and physical specifications for Hermes contrasted with typical aircraft values.

| Physical Metrics | System | | |
|---|---|---|---|
| | Boeing 737-700[40] | Cessna 172 Skyhawk[41] | Hermes |
| Length (m) | 33.6 | 8.3 | 0.125 |
| Span (m) | 35.8 (wing) | 11.00 (wing) | 0.0467 |
| Height (m) | 12.5 | 2.7 | 0.16 |
| Aspect ratio | 9.45 | 7.32 | 0.373 |
| Volume ($m^3$) | 107.6 (total cargo) | 0.85 (total cargo) | 2.75e-5 (total) |
| Weight (Kg) | 38,147 (operating empty weight) | 762 (operating empty weight) | 0.1342 (carbon fibre body) |

Hermes measures a total span of 4.67 cm with a volume of 27.5 cm$^3$ when used with 5 piezoelectric flags. The weight is governed largely by the manufacturing material. Using carbon fibre, a light weight composite used in aerospace applications, Hermes measures around 135 g which is over 1 M times smaller than a Boeing 737-Max and 5000x smaller than a Cessna 172. Hermes does not add any other overhead, thanks to its batteryless, self-powered, and wireless features. Further, unlike pressure-based *Pitot* probe styled sensors, it does not require any precision holes or tubes. The low form factor of Hermes as well as its wireless capability renders it adaptable to a wide range of fixed wing air crafts and UAVs with a constrained power budget.The form factor metrics of the sensor are summarised in Table 6.1

# 7

# Discussions

In this section, we elaborate on several features of Hermes and discuss how they can effectively be leveraged in practice.

## 7.1. Reliability

The small form factor of Hermes adds negligible weight or aerodynamic effects; thus, by deploying several redundant sensors, reliability can be increased. Currently used sensors rely on pressure tubes, called *Pitot* tubes, which need to be heated to prevent ice formation –*the main reason for Air France 447 crash*. On the contrary, due to its inherent flapping nature and the incoming wind, Hermes is less prone to ice formation. The unconventional physical phenomenon driving Hermes ensures variability in sensing mechanisms that safeguard the system during times of catastrophe. Indeed PVDF piezoelectric properties are temperature-dependent but it is linear, and the change in sensor readings can be easily corrected simply by adding a temperature sensor to the electronics at negligible cost. Thus the reliability of Hermes can be maintained over a wide range of operational conditions.

## 7.2. Enhancements to sensing range

Hermes is highly customizable to suit the sensing ranges required by the end applications. By translating the flutter characteristics of the piezoelectric flag into quantifiable features, we can estimate wind speed and AoA while harvesting sufficient energy for bending stiffness ranging from $K_b = 0.15$ to 0.10. The sensing range for AoA can easily be customized by choosing the appropriate number of piezoelectric flags, as described in Section 5. The range of wind speed, over which the sensor can function, requires altering the flutter range of the flags. This is possible by manipulating the dimensions as well as the physical properties of the flags used, namely Young's modulus and Poisson's ratio. In this work, we have demonstrated the high potential of Hermes using only the COTS piezoelectric films due to the unavailability of fabrication facilities in recent months. However, by using different film configurations, Hermes could be used to measure wide range of wind speeds.

We constructed our prototype using COTS piezoelectric films, and the wind tunnel capacity for evaluation also dictated our measurement range. The significance of Hermes in wind speed measurements is that it has a vast scope in changing the range of operation to suit the requirements imposed by the usecases (see Section 4). The power harvested and as a direct consequence, the communication range can be enhanced by changing the aspect ratio of the flags.

## 7.3. Customization for different applications

As mentioned above, the flag dimensions and material properties are key to the performance of Hermes under different flying conditions. Hermes in its current form and design can easily be mounted on smaller aircraft which fly at lower altitudes and have a maximum top speed of 55 knots. These aircraft are typically used for surveying or by hobbyists where an inexpensive, small-sized AoA sensor can add safety and aid the pilots for efficient flying. Hermes fulfills this niche. Since there is little provision for wiring in these aircraft, the prospect of wireless, self-powered sensing is very lucrative. It can also be utilized in fixed-wing drones and solar-powered UAVs with constrained power budgets. We can minimize power, cost, and size, which are highly sought after in these aircraft. Further, the applications of Hermes are not limited to aircraft or UAVs; it can be easily mounted and used in windmills, where accurate measurement of AoA could lead to better control and thus higher energy harvesting.

## 7.4. Batteryless operation

We use no battery to store generated energy. This is an important feature of Hermes since it is planned to be mounted as-is on the existing aircraft with the least modifications avoiding power requirement and wiring. Hermes, being batteryless, is highly pertinent for aircraft applications because it avoids the risks involved in using batteries near the wings and also its maintenance. A thorough study of the suitability of Hermes is required from the aerodynamics viewpoint, which is beyond the scope of this paper. The idea is to make Hermes as small as possible relative to the aircraft so that it is easy to use anywhere.

## 7.5. Limitations

While our work may open gateway to a plethora of applications in the area of sensing and harvesting, Hermes also has a few limitations. Firstly, the performance of Hermes was not evaluated under realistic flight conditions in the air because of restrictions. Secondly, although Hermes has tremendous potential – thanks to its design principles – to be applied in a wide variety of applications, the usage of COTS piezoelectric film and unavailability of fabrication facility in the recent months constrain us to test only a limited range of wind speed. In a follow-up work, we intend to overcome these limitations of Hermes.

# 8

# Related Work

Energy harvesting for sensor has been investigated earlier, e.g., [42]. Often the focus has been on optimizing the data collection schedules based on availability of harvested energy and harvesting opportunity [43] or on maximizing the utility operation of the network [44]. Most often energy harvesting and sensing functionalities are seen as conflicting, where choosing one translates to a sacrifice of the other rather than complementary where one reinforced the other [45, 46]. There have been some innovative investigations that synergized sensing and harvesting [47, 48]. The prospect of using piezoelectric materials solely for energy harvesting in sensor systems has been studied [49, 50] where the piezoelectric effect has been leveraged to generate energy, including wind-induced flutter. However, combined piezoelectric harvesting and sensing has not been addressed hitherto.

There have been some successful attempts that designed wind speed sensors being powered using micro-turbines [51] and piezoelectric materials [52]. These systems either cannot be adapted for aerospace applications or do not provide a mechanism for estimating wind speed independently without relying on a different sensor. While there are algorithms and signal processing techniques to find AoA using auxiliary sensors [53, 54] for UAVs and aircraft, there has not been much exploration in the space of self-powered AoA sensors. The investigations remain mostly around wired and battery-powered operations [55–57]. All these designs are inspired by standard Pitot tube designs or use even more conventional wind vane styled probes for AoA measurement. To the best of our knowledge, Hermes is unique, since it merges energy harvesting and sensing of two parameters. We compare and contrast our sensor Hermes with the current commercially available state of the art sensors.

Table 8.1 summarizes the performance and characteristics of this collation. From the comparison it is evident that this work is placed well as a redundant back up sensor to these state of the art sensors. We can harvest energy compared to these

Table 8.1: Comparison with state-of-the-art sensors

| | UTC Aerospace [16] | Aeroprobe [17] | Hermes |
|---|---|---|---|
| Form factor | 10.2 cm,<br>907.2 g | >20 cm,<br>>350g | 4.67 cm,<br>134.2 g |
| Type | AoA | AoA, Wind speed | AoA, Wind speed |
| Cost | > 5000 $ | > 5000 $ | 1̃50 $ |
| Power consumption | 1̃00W | 30 W | 440 $\mu$W |
| Sensing Accuracy | >1.5° | 1°,<br>1 m/s | 1.2°(90%)<br>0.2 m/s (90%) |

sensors making Hermes self powered. We can also measure both quantities, Angle of Attack and Wind speed simultaneously which eliminates the reliance of our sensor on other sensor and subsystems. It is also very evident from the table that we can match the state of the art both in terms of accuracy and range for sensing the Angle of Attack. We can do so with a cost that is an order of magnitude lower than the other two commercial sensors. Our design is also much smaller and lighter and thus multiple such sensors can be placed to further add redundancy and increase safety.

# 9

# Conclusion

Despite recent advancements in technology, there are still incidents of airline accidents as recent as last year, many of them primarily due to sensor failures. In this paper, we proposed a novel sensor, Hermes, which measured the Angle of Attack (AoA) and wind speed with appreciable accuracy. A compact array of piezoelectric films in Hermes produces a voltage under the aerodynamic phenomenon called flutter due to wind flow. Hermes is self-powered by harnessing the flutter (due to wind flow) to measure AoA and wind speed. We built a small form factor, proof of concept sensor that is batteryless, self-powered, and wireless. We proposed a new real-time algorithm to process the piezoelectric signals, enabling simultaneous measurement of AoA and wind speed. Further, flutter-based mechanical design also enabled simultaneous maximization of sensing performance and energy harvesting capability, without the need for the tradeoff. Hermes was evaluated through extensive wind tunnel experiments. We estimated the AoA and wind speed with an accuracy of $1.2^\circ$ and 0.2 m/s with $90\%$ probability, respectively. We also tested Hermes in a fuselage for packet reception ratios for different Tx power. Hermes can send two measurements every second when harvested energy is maximum, which is more than sufficient for most applications. The inexpensive, compact, and wireless design of Hermes enables a wide range of applications for piloted and unmanned flight systems, as well as other application such as wind farms. We have applied for a patent based on this work. The next step is to custom design the piezoelectric flags such that the operating range of wind speeds is enhanced.

# Supplementary Material

The author of this work is under the process of applying for a patent with TU Delft in The Netherlands. We however, do provide the resources and data collected in the development process of this sensor to aid the research and open source community. The videos of flutter, the wind tunnel experiment and fuselage experiment data are shared at: [58].

# References

## References

[1] *PZT Piezoelectric Energy Harvesters* (2009 (accessed June 1, 2020)).

[2] *Pvdf sensors,* (2017 (accessed June 1, 2020)).

[3] *MFC* (2017 (accessed June 1, 2020)).

[4] D. Winter, *Cyber-physical systems in aerospace-challenges and opportunities,* The Boeing Company , 14 (2011).

[5] A. Zolghadri, *Advanced model-based fdir techniques for aerospace systems: Today challenges and opportunities,* Progress in Aerospace Sciences **53**, 18 (2012).

[6] A. Levin and R. Beene, *Sensors linked to boeing 737 crashes vulnerable to failure,* (2020), accessed: 2020-8-10.

[7] D. D. Boyd, *Causes and risk factors for fatal accidents in non-commercial twin engine piston general aviation aircraft,* Accident Analysis Prevention **77**, 113 (2015).

[8] S. Jacobson, *Aircraft loss of control causal factors and mitigation challenges,* in *AIAA Guidance, navigation, and control conference* (2010) p. 8007.

[9] ICAO, *Flight departure statistics,* (2020), accessed: 2020-8-10.

[10] B.E.A, *Interim report on the accident on 1st june 2009 to the airbus a330-203 registered f-gzcp operated by air france flight af 447 rio de janeiro – paris,* (2020), accessed: 2020-8-10.

[11] I. N. T. S. C. (NTSC), *Pre- liminary aircraft accident investigation report: Lion air flight 610,* (2018), accessed: 2020-8-10.

[12] Boeing, *Aero 12: Angle of attack story,* (2020), accessed: 2020-8-10.

[13] A. Lambregts, G. Nesemeier, R. Newman, and J. Wilborn, *Airplane upsets: Old problem, new issues,* in *AIAA Modeling and Simulation Technologies Conference and Exhibit* (2008) p. 6867.

[14] F. Culick, *The wright brothers: first aeronautical engineers and test pilots,* AIAA journal **41**, 985 (2003).

[15] L. Sankaralingam and C. Ramprasadh, *A comprehensive survey on the methods of angle of attack measurement and estimation in uavs,* Chinese Journal of Aeronautics **33**, 749 (2020).

[16] U. A. Rosemount, *Model 0861h,* (2020), accessed: 2020-8-10.

[17] Aeroprobe, *Air data probe,* (2020), accessed: 2020-8-10.

[18] J. McCarthy, S. Watkins, A. Deivasigamani, and S. John, *Fluttering energy harvesters in the wind: A review,* Journal of Sound and Vibration **361**, 355 (2016).

[19] M. J. Shelley and J. Zhang, *Flapping and bending bodies interacting with fluid flows,* Annual Review of Fluid Mechanics **43**, 449 (2011).

[20] E. Naudascher and D. Rockwell, *Oscillator-model approach to theidentification and assessment offlow-induced vibrations in a system,* Journal of Hydraulic Research **18**, 59 (1980).

[21] E. Naudascher and D. Rockwell, *Flow-induced vibrations: an engineering guide* (Courier Corporation, 2012).

[22] T. Theodorsen, *General Theory of Aerodynamic Instability and the Mechanism of Flutter, NACA*, Tech. Rep. (TR 496, 1935).

[23] A. Kornecki, E. Dowell, and J. O'brien, *On the aeroelastic instability of two-dimensional panels in uniform incompressible flow,* Journal of Sound and Vibration **47**, 163 (1976).

[24] L. Huang, *Flutter of cantilevered plates in axial flow,* Journal of Fluids and Structures **9**, 127 (1995).

[25] D. Kim, J. Cossé, C. H. Cerdeira, and M. Gharib, *Flapping dynamics of an inverted flag,* Journal of Fluid Mechanics **736** (2013).

[26] S. Alben and M. J. Shelley, *Flapping states of a flag in an inviscid fluid: bistability and the transition to chaos,* Physical review letters **100**, 074301 (2008).

[27] B. S. Connell and D. K. Yue, *Flapping dynamics of a flag in a uniform stream,* Journal of fluid mechanics **581**, 33 (2007).

[28] S. Michelin, S. G. Llewellyn Smith, and B. J. Glover, *Vortex shedding model of a flapping flag,* Journal of Fluid Mechanics **617**, 1 (2008).

[29] J. Ryu, S. G. Park, B. Kim, and H. J. Sung, *Flapping dynamics of an inverted flag in a uniform flow,* Journal of Fluids and Structures **57**, 159 (2015).

[30] S. Orrego, K. Shoele, A. Ruas, K. Doran, B. Caggiano, R. Mittal, and S. H. Kang, *Harvesting ambient wind energy with an inverted piezoelectric flag,* Applied energy **194**, 212 (2017).

[31] W. G. Cady, *Piezoelectricity: Volume Two: An Introduction to the Theory and Applications of Electromechanical Phenomena in Crystals* (Courier Dover Publications, 2018).

[32] Q. Zhang, V. Bharti, and G. Kavarnos, *Poly (vinylidene fluoride)(pvdf) and its copolymers,* Encyclopedia of Smart Materials (2002).

[33] X. Shan, H. Tian, D. Chen, and T. Xie, *A curved panel energy harvester for aeroelastic vibration,* Applied Energy **249**, 58 (2019).

[34] J. Cossé, J. Sader, D. Kim, C. H. Cerdeira, and M. Gharib, *The effect of aspect ratio and angle of attack on the transition regions of the inverted flag instability,* in *Pressure Vessels and Piping Conference*, Vol. 46018 (American Society of Mechanical Engineers, 2014) p. V004T04A046.

[35] C. Huertas-Cerdeira, A. Goza, J. E. Sader, T. Colonius, and M. Gharib, *Dynamics of an inverted cantilever plate at moderate angle of attack,* arXiv preprint arXiv:2005.07374 (2020).

[36] L. Sigrist, A. Gomez, R. Lim, S. Lippuner, M. Leubin, and L. Thiele, *Measurement and validation of energy harvesting iot devices,* in *Proceedings of the 2017 Design, Automation Test in Europe Conference Exhibition (DATE 2017)* (Lausanne, Switzerland, 2017).

[37] *Piezo Film Product Guide and Price List*, MEASUREMENT SPECIALTIES, INC. (2008), rev. 1.

[38] N. Kong, D. S. Ha, A. Erturk, and D. J. Inman, *Resistive impedance matching circuit for piezoelectric energy harvesting,* Journal of Intelligent Material Systems and Structures **21**, 1293 (2010).

[39] *PIEZO FILM LAB AMPLIFIER*, MEASUREMENT SPECIALTIES, INC. (2017), rev. 1.

[40] Boeing, *737-700 design highlights,* (2020), accessed: 2020-8-10.

[41] Cessna, *Cessna skyhawk specifications,* (2020), accessed: 2020-8-10.

[42] K. S. Adu-Manu, N. Adam, C. Tapparello, H. Ayatollahi, and W. Heinzelman, *Energy-harvesting wireless sensor networks (eh-wsns): A review,* ACM Trans. Sen. Netw. **14** (2018), 10.1145/3183338.

[43] L. Yerva, B. Campbell, A. Bansal, T. Schmid, and P. Dutta, *Grafting energy-harvesting leaves onto the sensornet tree,* in *Proceedings of the 11th International Conference on Information Processing in Sensor Networks*, IPSN ’12 (Association for Computing Machinery, New York, NY, USA, 2012) p. 197–208.

[44] C. Renner, S. Unterschütz, V. Turau, and K. Römer, *Perpetual data collection with energy-harvesting sensor networks,* ACM Trans. Sen. Netw. **11** (2014), 10.1145/2566675.

[45] J. Hester and J. Sorber, *Flicker: Rapid prototyping for the batteryless internet-of-things,* in *Proceedings of the 15th ACM Conference on Embedded Network Sensor Systems*, SenSys '17 (Association for Computing Machinery, New York, NY, USA, 2017).

[46] M. Nardello, H. Desai, D. Brunelli, and B. Lucia, *Camaroptera: A batteryless long-range remote visual sensing system,* in *Proceedings of the 7th International Workshop on Energy Harvesting amp; Energy-Neutral Sensing Systems*, ENSsys'19 (Association for Computing Machinery, New York, NY, USA, 2019) p. 8–14.

[47] D. Ma, G. Lan, M. Hassan, W. Hu, M. B. Upama, A. Uddin, and M. Youssef, *Solargest: Ubiquitous and battery-free gesture recognition using solar cells,* in *The 25th Annual International Conference on Mobile Computing and Networking*, MobiCom '19 (Association for Computing Machinery, New York, NY, USA, 2019).

[48] S. DeBruin, B. Campbell, and P. Dutta, *Monjolo: An energy-harvesting energy meter architecture,* in *Proceedings of the 11th ACM Conference on Embedded Networked Sensor Systems*, SenSys '13 (Association for Computing Machinery, New York, NY, USA, 2013).

[49] M. Safaei, H. A. Sodano, and S. R. Anton, *A review of energy harvesting using piezoelectric materials: state-of-the-art a decade later (2008–2018),* Smart Materials and Structures **28**, 113001 (2019).

[50] Y. Han, Y. Feng, Z. Yu, W. Lou, and H. Liu, *A study on piezoelectric energy-harvesting wireless sensor networks deployed in a weak vibration environment,* IEEE Sensors Journal **17**, 6770 (2017).

[51] J. E. d. P. Braquehais and A. A. Lisboa de Souza, *Energy-autonomous wind speed smart sensor,* in *2014 IEEE International Instrumentation and Measurement Technology Conference (I2MTC) Proceedings* (2014) pp. 931–935.

[52] Y. Tan and S. Panda, *A novel piezoelectric based wind energy harvester for low-power autonomous wind speed sensor,* in *IECON 2007-33rd Annual Conference of the IEEE Industrial Electronics Society* (IEEE, 2007) pp. 2175–2180.

[53] T. A. Johansen, A. Cristofaro, K. Sørensen, J. M. Hansen, and T. I. Fossen, *On estimation of wind velocity, angle-of-attack and sideslip angle of small uavs using standard sensors,* in *2015 International Conference on Unmanned Aircraft Systems (ICUAS)* (2015) pp. 510–519.

[54] M. Oosterom and R. Babuska, *Virtual sensor for the angle-of-attack signal in small commercial aircraft,* in *2006 IEEE International Conference on Fuzzy Systems* (2006) pp. 1396–1403.

[55] Mi-Hyun Park, Sung-Su Kim, Chang-Kyung Ryoo, Keeyoung Choi, and Choonbae Park, *Development of alpha sensor for unmanned aerial systems,* in *2008 SICE Annual Conference* (2008) pp. 2131–2134.

[56] P. Pačes, K. Draxler, T. Čenský, V. Hanzal, and O. Vaško, *A combined angle of attack and angle of sideslip smart probe with twin differential sensor modules and doubled output signal,* in *SENSORS, 2010 IEEE* (2010) pp. 284–289.

[57] K. Wanngoen, N. Saetunand, W. Saengphet, and S. Tantrairatn, *Angle of attack sensor for small fixed-wing unmanned aerial vehicles,* in *Multidisciplinary Digital Publishing Institute Proceedings*, Vol. 39 (2020) p. 19.

[58] WhirlWind, *Whirlwind flutter video demonstration,* (2020), created: 2020-8-10.